

# Chapter 4

## Model Identification

The twenty-four parameters that define the concrete model must be determined using test data and common assumptions about concrete behaviors. If the model is to be used for a specific analysis, the ideal approach would be to fit the model using test data from the actual concrete being analyzed. However, if the model is to be used for predictive analysis, the exact behavior of the concrete will likely not be known before the analysis is performed. For this type of use, the parameters should be determined for some average concrete behavior that is able to represent typical concretes used in construction. Thus, a large quantity of test data with different types of confinement methods, concrete strengths, aggregate sizes, saturation levels, cross-sectional shapes, loading configurations, age, etc., were used to choose the values for the parameters. While it is clear that some of these variables will affect the strength and ductility of concrete, in many cases the values for these variables are not known at the time the analysis is performed. For example, the aggregate type used in the mix may not be known at the time of design, but would be known once the structure was constructed. Another example is the age of concrete, because the designer cannot know when the concrete will experience an extreme loading event. Therefore, it is necessary to obtain data with a wide range of values for these variables.

In typical structural applications, it is common to assume that the concrete is pre-cracked. Thus, for simplicity of the model as defined in this thesis, the pre-cracked assumption is used. This means that the yield, peak, and residual surfaces must all pass through the origin in the  $(\xi, r, \theta)$  invariant space. The yield surface meridians

are defined such that this criteria is already met. For the peak and residual surfaces, the pre-cracked assumption is used to define two of the parameters. In the case of all three surfaces, tension strength could easily be added at a later time, were it required.

This chapter describes how the values of the twenty-four parameters given in Table 3.1 were determined. The process for obtaining the parameters  $c$  and  $d$ , which define the yield surface, is discussed in Section 4.1. Determining the parameters for the peak surface—and the extensive test data used in that process—is discussed in Section 4.2. Similarly, the method for determining the residual surface is outlined in Section 4.3. The relationship used to define the damage increment,  $d\psi$ , and the determination of the value for  $\gamma$ , are discussed in Section 4.4. Finally, the determination of the parameters relating to the flow rule and the location of the failure surface are discussed in Section 4.5.

## 4.1 Yield Surface Definition

The equations that define the yield surface have only two parameters. As discussed in Section 3.1.1, the precise location of the yield surface is not critical since the onset of concrete yielding occurs gradually. Thus, the parameter  $d$  was determined by assuming that the yield point of uniaxially loaded concrete is 45% of the peak stress. This assumed yield point for concrete is commonly used [for example, Malvar et al. (1994)]. The stress state at uniaxial yield is given by:

$$\left. \begin{aligned} \sigma_x = \sigma_y = 0 \\ \sigma_z = (-0.45)f'_c \end{aligned} \right\} \text{at uniaxial yield} \quad (4.1)$$

Equation 4.1 corresponds to the invariant values:

$$\left. \begin{aligned} \xi &= -\frac{0.45f'_c}{\sqrt{3}} \\ r &= 0.45\sqrt{\frac{2}{3}}f'_c \\ \theta &= 60^\circ \end{aligned} \right\} \text{at uniaxial yield} \quad (4.2)$$

Implementing this stress state into Equation 3.4 for the yield surface gives a value for the parameter  $d$ :

$$d = 0.45\sqrt{\frac{2}{3}}\left(1 + \frac{\sqrt{3}}{0.45}\right) \simeq 1.78 \quad (4.3)$$

Similarly, data from Kupfer et al. (1969) indicate that biaxial loading of concrete results in a 16% increase in concrete stress when a specimen is loaded biaxially. Thus, it is assumed that a specimen loaded biaxially will yield at 45% of a peak stress increased by 16%. This corresponds to the stress state given by:

$$\left. \begin{aligned} \sigma_x &= 0 \\ \sigma_y &= \sigma_z = -(0.45)(1.16)f'_c \end{aligned} \right\} \text{at biaxial yield} \quad (4.4)$$

Equation 4.4 corresponds to the invariant values:

$$\left. \begin{aligned} \xi &= -\frac{(2)(0.45)(1.16)f'_c}{\sqrt{3}} \\ r &= (0.45)(1.16)\sqrt{\frac{2}{3}}f'_c \\ \theta &= 0^\circ \end{aligned} \right\} \text{at biaxial yield} \quad (4.5)$$

Implementing this stress state into Equation 3.4 for the yield surface gives a value for the parameter  $c$ :

$$c = (0.45)(1.16)\sqrt{\frac{2}{3}}\left(1 + \frac{\sqrt{3}}{(2)(0.45)(1.16)}\right) \simeq 1.13 \quad (4.6)$$

The parameters  $c$  and  $d$  uniquely define the yield surface. These values for the parameters, defined in Equations 4.3 and 4.6, respectively, were used to validate the model (Chapter 6) and predict concrete behavior (Chapter 7).

In summary, a simplified approach was taken to define the yield surface since it is not critical in predicting the effect of confinement on concrete. The remaining components of the model capture the important behaviors of concrete under confinement. Parameters pertaining to those components will be determined in a more rigorous fashion in the following sections.

## 4.2 Peak Surface Correlation

A total of twenty-one data sets, published in twenty-seven papers, were obtained to estimate the parameters defining the peak surface. The tests performed in each of the published studies were intended to study the effects of confinement on the behavior of concrete. Several of the authors designed their experiments to test the effects of certain variables on confined concrete behavior. Other papers only test a single concrete mix at different confinement levels, but can be compared to similar papers to understand the effect of different concrete variables. With the compilation of all twenty-one data sets, a large number of concrete variables were taken into consideration.

Several concrete mix variations were tested in the different papers. The concrete age at testing varied from 10 to 200 days. Water-cement ratios of 0.26 to 1.25 were used. Several different additives were considered, including fly ash, silica fume, superplasticizers, air-entraining agents, and water-reducing agents. The type, weight, surface roughness, and size of the aggregates varied widely throughout the studies. A maximum coarse aggregate size range of 0.375 to 1.5 inches (9.5 to 38 mm) was seen throughout the papers, and some mixes did not include any coarse aggregate, only sand. The proportions of water/cement/sand/aggregate were varied over a large range. The saturation level was varied from oven dried to 100% saturated and immersed in fluid at the time of testing. The final concrete compressive strength in the tests varied from 1.1 to 19.1 ksi (7.5 to 132 MPa)

Test setup details created other variables within the tests. Specimen sizes and shapes ranged from 2.125 x 4.25 inch (54 x 108 mm) cylinders, 5 x 5 x 0.5 inch (125 x 125 x 12.5 mm) plates, and 2.25 x 2.25 x 2.25 inch (57.2 x 57.2 x 57.2 mm) cubes up to 12 x 14 inch (305 x 350 mm) cylinders, 7.9 x 7.9 x 2 inch (200 x 200 x 50 mm) plates, and 4 x 4 x 4 inch (100 x 100 x 100 mm) cubes. The load paths varied over Lode angles from 0° to 60°, and failure was approached from multiple different directions. Two papers detailed experiments with different friction reducing boundary conditions including dry steel platens, one or two 0.08 in (2 mm) thick resin sheets

both ungreased and greased, teflon greased teflon pads, and polyester film greased aluminum pads.

The method of testing was varied utilizing different methods of lateral load application including active and passive confinement and biaxial and triaxial loading. Passive tests included several different types of confining materials including steel rebar and glass and carbon fiber reinforced polymer (FRP). The number and strength of the FRP wraps was varied as well as the diameter, spacing, and yield strength of the steel rebar.

The compilation of the data represents a wide range of a large number of important concrete variables, which is critical to representing a wide variety of different concrete and loading conditions. Details of each paper contributing data used for the peak surface are discussed in Section 4.2.1. The compilation of the data is shown and discussed in Section 4.2.2. Finally, the fit for the peak loading surface is discussed in Section 4.2.3.

### **4.2.1 Peak Surface Papers**

Table B.1 gives a summary of the twenty-one data sets. Discussion of the papers is divided based on the loading configuration. Though the papers are discussed and separated by loading configuration, all data were used together for estimating the parameters. The other variables tested will be highlighted in the discussion of each individual paper.

Twelve of the data sets used a triaxial pressure vessel, or Hoek cell, for loading. Details of this type of machine are discussed extensively elsewhere [for example, MTS Systems Corporation (2004), Hoek and Franklin (1968), and Blanks and McHenry (1945)]. To summarize, the specimen to be tested is placed in a traditional universal testing machine for the axial loading. However, the cylinder is enclosed by a fluid-filled pressure chamber and sheathed in rubber, neoprene, plastic, or similar casing to prevent the fluid from penetrating the specimen. In this way, the specimen has a constant, controlled lateral pressure throughout the duration of the loading. In these

types of tests, hydrostatic pressure means that equal loads are applied axially (by the universal testing machine) and laterally (by the fluid). A typical example of this type of machine is shown in Figure 4.1. Use of this type of machine proves an ideal

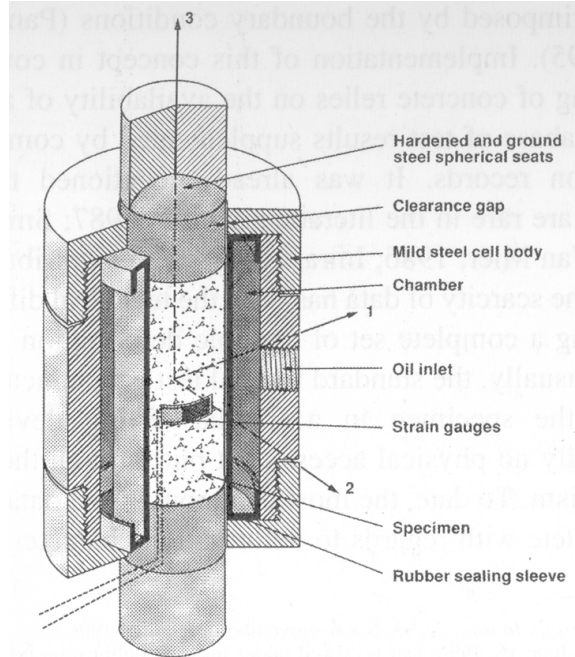


Figure 4.1: Example of a triaxial pressure vessel. Reproduced from Imran and Pantazoulou (1996).

way to test the effect of confinement on different types of concrete. For this reason, the majority of the data sets chosen used this method. These papers are discussed in Section 4.2.1.1. The limitation of this setup is the inability to have intermediate values for the Lode angle. The Lode angle is either  $0^\circ$  or  $60^\circ$ , based on whether the fluid pressure exceeds the axial load being applied.

Four papers were chosen that tested concrete cubes under true triaxial loading, allowing for the full range of Lode angles to be tested. These researchers utilized a triaxial device that had the ability to apply loads along each of the three axes independently. The four true triaxial papers are detailed in Section 4.2.1.2. The machine utilized for each set of experiments is discussed in the individual papers. The typical setup was to use three independent hydraulic rams to apply loads in the three orthogonal directions of the cubic specimen. An example of this type of

machine is shown in Figure 4.2. The challenge with this type of loading is to ensure the

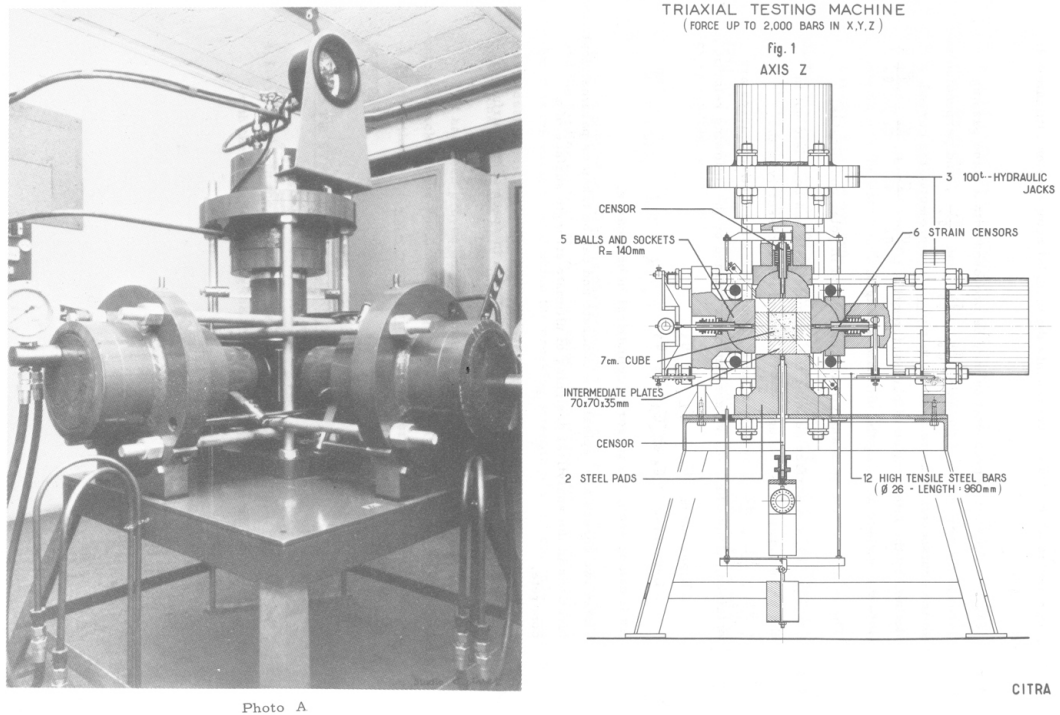


Figure 4.2: Example of a true triaxial testing machine. Reproduced from Launay and Gachon (1972a).

proper friction reducing boundary condition. The approach to avoid these boundary condition effects is discussed in each individual paper.

Three papers were chosen that used passive confinement. Two of these utilized steel rebar or wire, the third used fiber reinforced composite sheets. Equations were presented in each paper to estimate lateral pressure as a function of the confinement configuration. Those equations were used in this thesis when calculating the lateral pressure on the specimen at peak stress. The papers are summarized in Section 4.2.1.3.

Finally, two papers were selected that performed traditional biaxial tests. Biaxial testing has the same challenges as true triaxial loading in regards to minimizing the effects of the boundary conditions. Biaxial papers are discussed in Section 4.2.1.4.

#### 4.2.1.1 Peak Surface Papers Utilizing a Triaxial Pressure Vessel

A set of papers were published by Q. Li and F. Ansari detailing their experiments [(Ansari and Li, 1998), (Li and Ansari, 1999), (Li and Ansari, 2000)]. A modern triaxial pressure vessel (MTS Systems Corporation, 2004) was used for these tests. Concrete cylinders were enclosed in a rubber membrane for testing. The confinement effect of this membrane, leading to an average 7% increase in axial strength, was taken into account in the results. Three high strength mixes with  $f'_c$  values of 6.9, 10.3, and 15.6 ksi (47.7, 71.1, and 107.3 MPa) were tested in Ansari and Li (1998) and Li and Ansari (1999), while only the two higher strength mixes were tested in Li and Ansari (2000). A comparison of specimen sizes was performed by using 4 x 8 inch (100 x 200 mm) cylinders in Ansari and Li (1998) and Li and Ansari (1999), while 3 x 6 inch (76 x 152 mm) cylinders were used in Li and Ansari (2000). Specimens in Ansari and Li (1998) and Li and Ansari (1999) were tested at an age of  $40 \pm 7$  days. Specimens in Li and Ansari (2000) were tested at an age of  $35 \pm 7$  days. In both cases, the specimens were moist cured until the day before testing. Specimens were hydrostatically loaded to the desired lateral confining pressure, then the axial load was increased to failure. Confinement pressures ranging from  $0.18f'_c$  to  $0.93f'_c$  were applied. The authors concluded that the influence of confining pressure on the failure strength of high strength concrete is not as pronounced as with normal strength concrete. However, there is a large and distinct increase in the failure strain of high strength concrete due to confinement. Results of the final paper were used to conclude that high strength concrete has a minor size effect, but it is not necessary to take it into account when modeling failure surfaces.

Attard and Setunge (1994) and Attard and Setunge (1996) used five different concrete mixes with three different coarse aggregate types leading to eleven different cylinder strengths, with  $f'_c$  values ranging from 8.4 to 19.1 ksi (58 to 132 MPa). The 4 x 8 inch (100 x 200 mm) cylindrical specimens were moist cured at 100% humidity until 7 days before testing, then air dried to reduce the influence of pore water pressure on the results. Most of the specimens were tested at 90 days after casting. Confining

pressures ranging from 72.5 to 2900 psi (0.5 to 20 MPa) were applied to the cylinders through the pressurized fluid. The authors concluded that the type of aggregate used had a significant influence on the elastic modulus, strain at peak stress, and ductility.

Balmer (1949) used the then recently constructed triaxial pressure vessel (Blanks and McHenry, 1945) for his experiments. The 6 x 12 inch (152 x 305 mm) cylindrical specimens were all cast from the same mix, fog-cured for 28 or 90 days, then oven dried for 7 days. The 28 and 90 day specimens had unconfined strengths of 3.6 and 4.0 ksi (25 and 28 MPa), respectively. Confining pressures from 1 to 25 ksi (7 to 172 MPa) were applied through the use of pressurized kerosene. The specimens were encased in rubber jackets. The author concluded that the increase in strength with confinement was nonlinear.

Bellamy (1961) used both solid and hollow cylinders in his testing. The cylinders were 6 x 12 inches (152 x 305 mm) in size, and the hollow cylinders had an inner diameter of 2.95 inches (74.9 mm). Specimens were fog cured at 100% humidity for 7 days and then stored at 80% humidity until testing at an approximate age of 200 days. The solid cylinders were tested to determine the increase in strength and strain at failure due to triaxial loading. The hollow cylinders were used to investigate biaxial loading. Failure always initiated at the inside face of the hollow cylinders where the concrete was in a biaxial stress state. Both types of cylinders were hydrostatically loaded to the desired lateral pressure, then the axial load was increased to failure. The comparison of the two different loading types was used to draw some conclusions about the effect of the Lode angle. The author concluded that the intermediate principal stress increased the major principal stress at failure by a minimum of 75%.

Tests performed by Candappa, Setunge, and Sanjayan investigated the complete stress versus strain curves of high strength concrete [(Candappa et al., 1999), (Candappa et al., 2001)]. The 4 x 8 inch (100 x 200 mm) cylinders were placed in a thin polyurethane membrane, and the lateral confining pressure was applied through the use of oil. Three high strength mixes and one normal strength mix were tested. Cylinders were cured for 28 days in standard bath conditions, then allowed to air dry for at least 28 days before testing. At the time of testing, cylinder strengths

( $f'_c$ ) of the four mixes were 6.1, 8.8, 10.6, and 15.0 ksi (41.9, 60.6, 73.1, and 103.3 MPa). Confining pressures of 0.6, 1.2, and 1.7 ksi (4, 8, and 12 MPa) were tested. Specimens were loaded laterally to the desired confinement level and then the axial load was increased to failure. The authors concluded that the axial strain at peak stress showed a linear relationship with confinement. They also noted that the effect of confinement on strains at peak stress appears less for high strength concrete under higher confinement levels.

Chinn and Zimmerman (1965) used the same triaxial pressure vessel as Balmer (1949), but specimens were loaded to much higher confining pressures. Four different loading paths were tested. Type one loading, similar to other papers, was to load the specimen hydrostatically to the desired confining pressure, then increase the axial load to failure. Confining pressures for this load type varied from  $0.5f'_c$  to  $17.1f'_c$ . Type two was to load the specimens hydrostatically to the desired axial pressure and then increase the confining pressure to failure. Axial loads ranged from 0.0 to  $3.7f'_c$ , while final lateral pressures ranged from  $1.4f'_c$  to  $11.5f'_c$ . These two loading types were performed to examine the effect of the two extreme values for the Lode angle at various confinement levels. Type three was pure hydrostatic loading to the capacity of the testing machine. Type four was to increase lateral stresses as a constant proportion of the axial stress until the specimen failed. Final confining pressures for this loading varied from  $2.2f'_c$  to  $12.2f'_c$ . During testing, the 6 x 12 inch (152 x 305 mm) cylinders were encased in either a neoprene or polyvinylchloride sheath. Three concrete mixes were arbitrarily selected with target compressive strengths of 4, 7, and 10 ksi (28, 48, and 69 MPa). Due to variations in the mixture and casting methods, the actual  $f'_c$  values varied from 3.4 to 10.3 ksi (23 to 71 MPa). Specimens were cured for 7 days and then oven dried for 24 hours. Due to issues with the testing machine, the specimens were then stored in the lab for 1 to 10 days before being tested. Both type one and type two loading showed a linear increase in strength with confinement. However, the slope of this line was 1.0 for type one and 2.1 for type two. By comparing type four loading with type one, it was noted that the load path did not affect the final stress state of the specimen at failure.

Cordon and Gillespie (1963) undertook an extensive investigation of the effects of different aggregates and cements on the strength of concrete. Eighteen different concrete mixes were made for triaxial testing with water-cement ratios of 0.40, 0.55, and 0.70 with 0.75 and 1.5 inch (19 and 38 mm) maximum coarse aggregate sizes. Final  $f'_c$  values ranged from 5.7 to 6.6 ksi (39 to 46 MPa), with slumps ranging from 1 to 8 inches (25 to 200 mm). The 6 x 12 inch (152 x 305 mm) cylinders were encased in thin plastic bags and tested at confinement pressures ranging from  $0.05f'_c$  to  $1.13f'_c$ . The authors concluded that water-cement ratio is not the sole important variable in establishing the strength of the concrete; the maximum size, surface texture, and shape of the aggregate are also important.

Duke and Davis (1944) studied the effect of saturation on the creep and triaxial strength of concrete. Saturated specimens were moist cured for 28 days before testing and were in direct contact with the water used to apply the lateral loads during testing. Partially-dry specimens were moist cured for 21 days, moved to 50% humidity for 5 days, and then coated with a heavy moisture-resistance lacquer for testing. Saturated specimens had a compressive strength,  $f'_c$ , of 5.7 ksi (39 MPa), while the partially-dry specimens had a compressive strength,  $f'_c$ , of 6.6 ksi (46 MPa). Lateral pressures of 0 to 900 psi (0 to 6 MPa) were applied to the 3 x 6 inch (76 x 152 mm) cylinders. Test results indicated that while the strength of the saturated specimens was lower, the strength increase due to lateral confinement was the same for saturated and partially-dry specimens.

Imran and Pantazopoulou (1996) investigated the effects of saturation, water-cement ratio, and load path on the triaxial behavior of concrete. Cylinders were encased in a urethane rubber membrane for testing in the triaxial pressure vessel. Lateral stresses of  $0.05f'_c$ ,  $0.10f'_c$ ,  $0.20f'_c$ ,  $0.40f'_c$ ,  $0.70f'_c$ , and  $1.0f'_c$  were applied to the 2.125 x 4.25 inch (54 x 108 mm) cylinders. Water-cement ratios of 0.40, 0.55, and 0.75 were used. Saturated specimens were moist cured for approximately 3.5 months before testing, leading to concrete strengths of 3.1, 6.3, and 9.4 ksi (21.2, 43.5, and 64.7 MPa). Dry specimens were also moist cured for approximately 3.5 months, but then dried at 140°F (60°C) for 72 hours before testing. Final concrete strengths of the

dry specimens at testing were 4.2, 6.9, and 10.6 ksi (28.6, 47.4, and 73.4 MPa). Four load paths were considered. Type A loading applied the desired confining pressure while the axial load remained zero and then increased the axial load to failure. Type B loading alternated between increasing the confining pressure and the axial load in increments until failure was reached. Type C loading applied a specified confining pressure and then decreased the confining pressure and increased the axial load in increments until failure was reached. Type D loading applied the lateral pressure then cycled the axial load. The authors made several important conclusions. Failure of the concrete specimens tested triaxially was defined by the initiation of volumetric expansion. Saturated concrete specimens exhibited lower strength than comparable dry specimens. This weakening was more pronounced for concretes with a higher water-cement ratio. Concrete loaded cyclically exhibited a degradation in elastic modulus which led to some path dependence of the deformation behavior. Cyclically loaded specimens also exhibited higher volumetric expansion at the same level of axial deformation. However, the peak strength of the concrete was observed to be path independent.

Richart, Brandtzaeg, and Brown performed the pioneering work in the study of the triaxial behavior of concrete in their two papers, Richart et al. (1928) and Richart et al. (1929). The latter paper tested passively confined columns and will be discussed in Section 4.2.1.3. The former paper studied the effect of confinement on the strength and ductility of concrete through the use of a triaxial pressure vessel. Three different mixes were tested triaxially. The three mixes, with water-cement ratios of 0.64, 0.88, and 1.25, yielded final  $f'_c$  values of 1.1, 2.6, and 3.7 ksi (7.6, 18, and 26 MPa). The 4 x 8 inch (100 x 200 mm) and 4 x 22 inch (100 x 560 mm) cylinders were moist cured for approximately 27 days, then were typically allowed to air dry about one day before testing. Lateral confining pressure ranged from  $0.07f'_c$  to  $5.71f'_c$ . Due to many problems with the testing equipment, the authors were only able to conclude that the strength of concrete is significantly raised through confinement. However, the variation with Lode angle was uncertain.

Rosenthal and Glucklich (1970) studied the biaxial behavior of concrete using

hollow cylinders in a triaxial pressure vessel. The 12 x 14 inch (305 x 350 mm) cylinders had an inner diameter of 9.8 inches (250 mm). Two concrete mixes, with water-cement ratios of 0.63 and 0.94, yielded compressive strengths at testing ranging from 2.8 to 6.9 ksi (20 to 48 MPa). The specimens were stored for 7 days under water, then for another 75 days at 65% humidity. Testing took place at an age of 90 days. The authors concluded that the initiation of failure in the concrete is through the initiation of internal cracking. They noted that by increasing the mean stress, the concrete was able to delay the onset of internal cracking to a higher load.

Sfer et al. (2002) studied the effect of age on the behavior of concrete under triaxial compression. One mix of concrete was used with a water-cement ratio of 0.57. The 6 x 12 inch (150 x 300 mm) cylinders were moist cured until tested. The cylinders were placed in a butyl sleeve, with a neoprene sleeve fitted over it, before being placed in the pressure vessel. One series of tests was performed at an age of  $60 \pm 9$  days with a concrete compressive strength at testing of 4.8 ksi (32.8 MPa). The second series of tests, identical to the first, was performed at an age of  $100 \pm 15$  days with a concrete compressive strength at testing of 5.6 ksi (38.8 MPa). Lateral pressures ranging from  $0.04f'_c$  to  $1.83f'_c$  were tested. By comparing the results with other tests, the authors concluded that the results were independent of specimen size. They also noted that by increasing the confining pressure, the failure of the specimens transitioned from a brittle to a ductile failure.

#### **4.2.1.2 Peak Surface Papers Utilizing a True Triaxial Testing Machine**

Chuan-zhi et al. (1987) studied the effects of different friction reducing boundary conditions on true triaxial testing. Four different friction-reducing pads were compared in the testing. Two mixes with two different coarse aggregates were used to cast the 4 x 4 x 4 inch (100 x 100 x 100 mm) cubes with concrete strengths ranging from 1.1 to 2.1 ksi (7.5 to 14.3 MPa). Specimens were tested both biaxially and triaxially, with lateral confinement pressures ranging from  $0.06f'_c$  to  $3.43f'_c$  for the biaxial loading and  $0.10f'_c$  to  $4.20f'_c$  for the triaxial testing. The authors concluded that the Lode angle significantly affects the peak strength of the triaxially loaded specimens.

Lan and Guo (1997) investigated the effect of the load path on the multiaxial behavior of concrete. One concrete mix was used with a water-cement ratio of 0.71. The specimens were cast in four batches with  $f'_c$  values ranging from 2.2 to 3.8 ksi (15.0 to 26.5 MPa). The 2.78 x 2.78 x 2.78 inch (70.7 x 70.7 x 70.7 mm) cubes were moist cured for 28 days, then placed in air until testing. Four biaxial and two triaxial loading paths were considered. Details of the biaxial load paths can be found in the cited paper. The first triaxial load path was to hydrostatically load the cube and then decrease the axial load to failure. The second triaxial load path was to apply the two lateral loads to the desired value and then increase the axial load to failure. The authors concluded that, in practice, the biaxial strength of concrete is independent of the load path. By comparing the triaxial results of these experiments with triaxial results of other papers which utilized a different load path, the authors concluded that the triaxial strength of concrete is also load independent.

Launay and Gachon (1972a) and Launay and Gachon (1972b) performed triaxial tests on a concrete intended for use in a nuclear reactor. The mix for this concrete used a water-cement ratio of 0.53, creating a final compressive strength of 5.2 ksi (36 MPa). Cubes 2.76 x 2.76 x 2.76 inches (70 x 70 x 70 mm) were cured under water for 7 days and were then stored in a tight polyethylene sack until testing at 28 days. Specimens were tested at lateral pressures ranging from  $0.20f'_c$  to  $5.64f'_c$ . The results included a fairly wide range of both the Lode angle and confinement levels.

Mills and Zimmerman (1970) also studied different friction reducing boundary conditions under uniaxial testing then utilized the best boundary pads to investigate the multiaxial behavior of concrete. Three different mixes with water-cement ratios of 0.49, 0.58, and 0.66 were used to cast the 2.25 x 2.25 x 2.25 inch (57.2 x 57.2 x 57.2 mm) cubes. Final compressive strengths of 3.3, 3.9, and 5.2 ksi (23, 27, and 36 MPa) were reached in the concrete. The cubes were moist cured for 28 days, then allowed to dry for approximately one month before testing. All stresses were applied hydrostatically until a particular direction had reached the desired level, at which point only the other directions continued to increase. This continued until failure of the specimen. Lateral stresses ranging from  $0.02f'_c$  to  $3.14f'_c$  were applied

to the cubes. A wide range of Lode angles was tested. The authors noted that the failure planes appeared in the plane or planes of the minimum principal stress. They also noted that the effect of the Lode angle was significant and should be taken into account when creating failure criteria.

#### **4.2.1.3 Peak Surface Papers Utilizing Passive Confinement**

Ahmad and Shah (1982) tested spirally-reinforced concrete cylinders. Seven series of tests were utilized: five with normal weight concrete, all of the same mix; two with lightweight concrete, each with its own mix. Cylindrical specimens 3 x 6 inches (75 x 150 mm) in size were stored at 100% humidity until 1 to 2 days before testing, when conditions were changed to 50% humidity. The age of the specimens at testing was varied from 28 to 200 days so as to have a variety of compressive strengths ranging from 3.8 to 9.5 ksi (26 to 65 MPa). The spiral pitch, diameter, and yield strength were varied for the eight different series. The authors concluded that an increase in compressive strength or use of lightweight aggregate decreases the effectiveness of confinement.

Toutanji (1999) studied the behavior of concrete columns wrapped in varying levels of FRP composite sheets. The 3 x 12 inch (76 x 305 mm) cylindrical specimens were all cast from the same mix, having a water-cement ratio of 0.5. The final compressive strength of the plain cylinders was 4.5 ksi (30.9 MPa). The cylinders were confined with two wraps of a unidirectional FRP sheet. Three types of fibers were used for the sheets, two carbon and one glass, which were bonded with the same type of epoxy system. The confined cylinders were then loaded in uniaxial compression to failure. The authors concluded that the compressive strength, maximum strain, and ductility were all significantly increased through the use of FRP confinement. The increase in strength of the specimens confined with carbon fiber was higher due to the higher lateral stresses supported by the carbon fiber, which had a higher elastic modulus and tensile strength.

Richart et al. (1929) tested concrete passively confined by steel wire or bar. Only one mix was tested, with a water-cement ratio of 0.87, and all specimens were 10 x

40 inch (254 x 1016 mm) cylinders. Cylinders were stored in the lab in wet burlap for 24 days to cure. Two days before testing, the burlap was removed and the cylinders were prepared for testing. Testing variables included only the amount and kind of spiral reinforcement. Two different sized mild steel drawn wires, three different sized mild steel rolled bars, and one high strength cable steel stock were used for reinforcement. Only one pitch was tested for each size of each steel type. Thus, six different reinforcement ratios were tested. The authors concluded that, within the range of confinement found by steel spirals, the increase in the strength of concrete was linear with confinement pressure.

#### **4.2.1.4 Peak Surface Papers Utilizing Biaxial Loading**

Calixto (2002) performed biaxial tension-compression loading. Specimens were 5 x 5 x 0.5 inch (125 x 125 x 12.5 mm) plates cast from the same high strength mix. The plates were cured at 100% humidity for 56 days, then removed and prepared for testing. The compressive strength of the plates at testing was 8.6 ksi (59.6 MPa), while comparable cylinder tests showed a compressive strength of 10.8 ksi (74.4 MPa). This difference was attributed to the lack of confinement existing in the plate specimens. The author noted that the shape of the strength envelope for high strength concrete is much more linear than that obtained for normal strength concrete. Further, the decrease in the compressive strength under biaxial tension-compression is lower for normal strength concrete than for high strength concrete.

Kupfer et al. (1969) and Kupfer and Gerstle (1973) performed a series of biaxial tests. Three concrete mixes with water-cement ratios of 0.43, 0.90, and 1.20 were used. Specimens were moist cured for 7 days, then stored at 65% humidity for 21 days. Final compressive strengths,  $f'_c$  values, of 2.77, 4.51, and 8.62 ksi (19.1, 31.1, and 59.4 MPa) were reached by the concrete. The 7.9 x 7.9 x 2.0 inch (200 x 200 x 50 mm) plates were tested at four different stress ratios: biaxial tension, tension-compression, and two biaxial compression states. The authors noted an average increase in strength of 16% when the specimens were loaded with equal compressive stresses in two principal directions.

## 4.2.2 Peak Surface Data

Figures 4.3 and 4.4 show all test data for Lode angles of  $0^\circ$  and  $60^\circ$  which correspond to the peak tensile and compressive meridians, respectively. Note that compression is defined as negative. Plots for each individual set of experiments are shown in Appendix C.

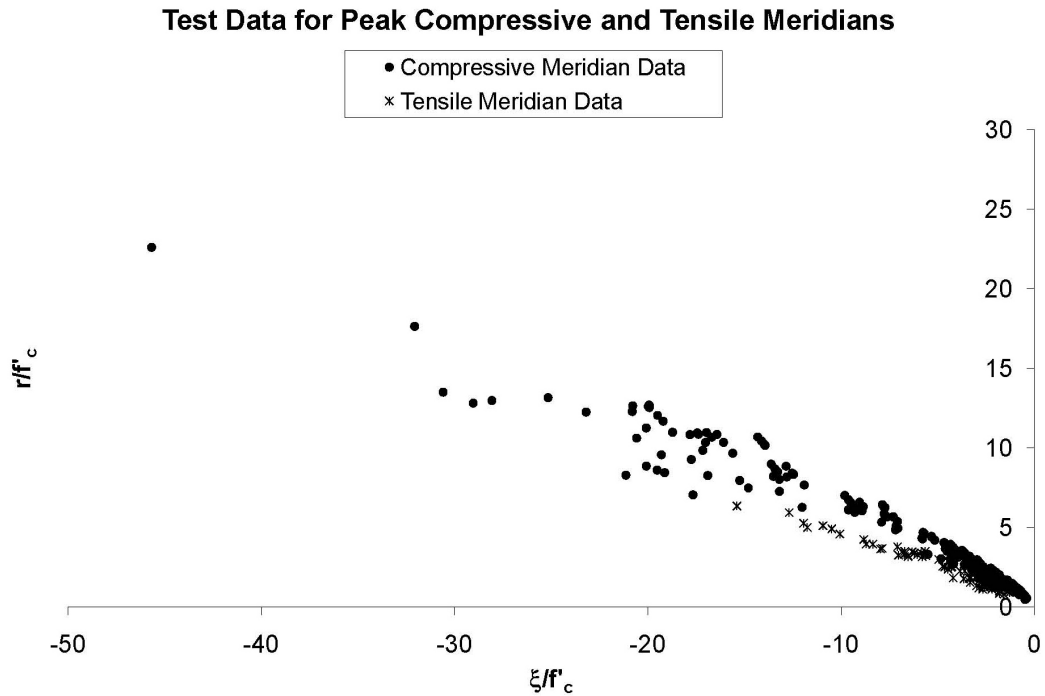


Figure 4.3: Test data for peak compressive and tensile meridians.

It is observed that some of the data at a Lode angle of  $60^\circ$  actually overlap with data for a Lode angle of  $0^\circ$ . The multiaxial loading configuration that corresponds to the strongest state for a concrete specimen is a Lode angle of  $60^\circ$ . If there exists some problem within the test setup, the concrete will soften prematurely, and the experimentally determined peak stress state will lie below the true peak stress state of the concrete. From all data sets, it is apparent that a Lode angle of  $0^\circ$  corresponds to a lower deviatoric stress,  $r$ , for the same hydrostatic stress,  $\xi$ . Authors that investigated the effect of the Lode angle on concrete behavior previously noted this from individual tests. Thus, a problem with the test setup could cause some data points for a Lode angle of  $60^\circ$  to be smaller and in the range of data for a Lode angle

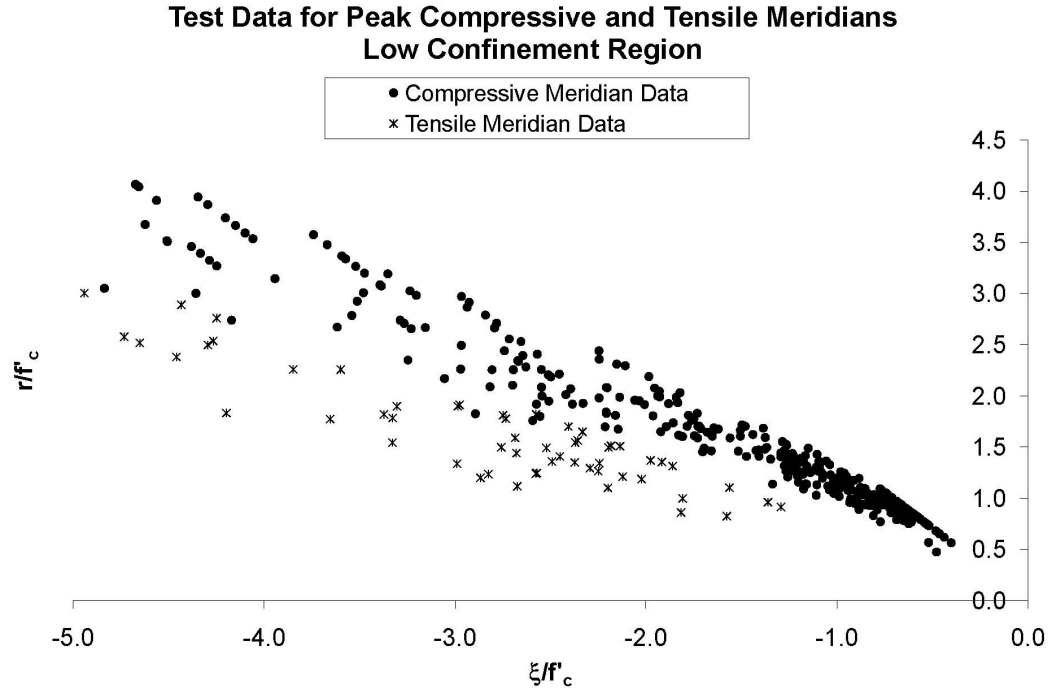


Figure 4.4: Test data for peak compressive and tensile meridians: low confinement region.

of  $0^\circ$ .

There are several ways in which testing problems can lead to premature concrete failure. For example, for concrete specimens loaded in a triaxial pressure vessel, failure often led to puncturing of the protective sheath and penetration of the fluid. However, there is no way to be certain that the sheath was not ruptured prematurely, leading to penetration of the fluid. The dramatic increase in pore pressure due to penetration of the fluid into the pores of the specimen would alter the stress state in the concrete, similar to the effective stress concept in soils. This penetration of the fluid could cause premature failure of the specimen. Thus, there may be some ambiguity as to whether the true peak strength of the concrete was reached. Similarly, for true triaxial testing, if the boundary conditions are not frictionless, additional stresses introduced at the boundary could affect failure of the specimen. For these reasons, it is understood why there exists some data points corresponding to a Lode angle of  $60^\circ$  which may lie somewhat below the compressive meridian. Problems with the testing conditions will typically cause the specimen to fail at a stress state less than the true peak. This

is an important point in understanding the scatter seen in the data.

As previously mentioned, it was the intent to gather data with a large variation in concrete and testing variables. Bringing this large quantity of data together allows for the investigation into the effects of these variables on concrete behavior. The effects of the concrete compressive strength, the confinement method, the specimen size, and the year of testing are explored in the following figures.

Figures 4.5 and 4.6 show the spread in the peak compressive meridian data due to the value of  $f'_c$  for that concrete specimen. It is widely accepted that concrete

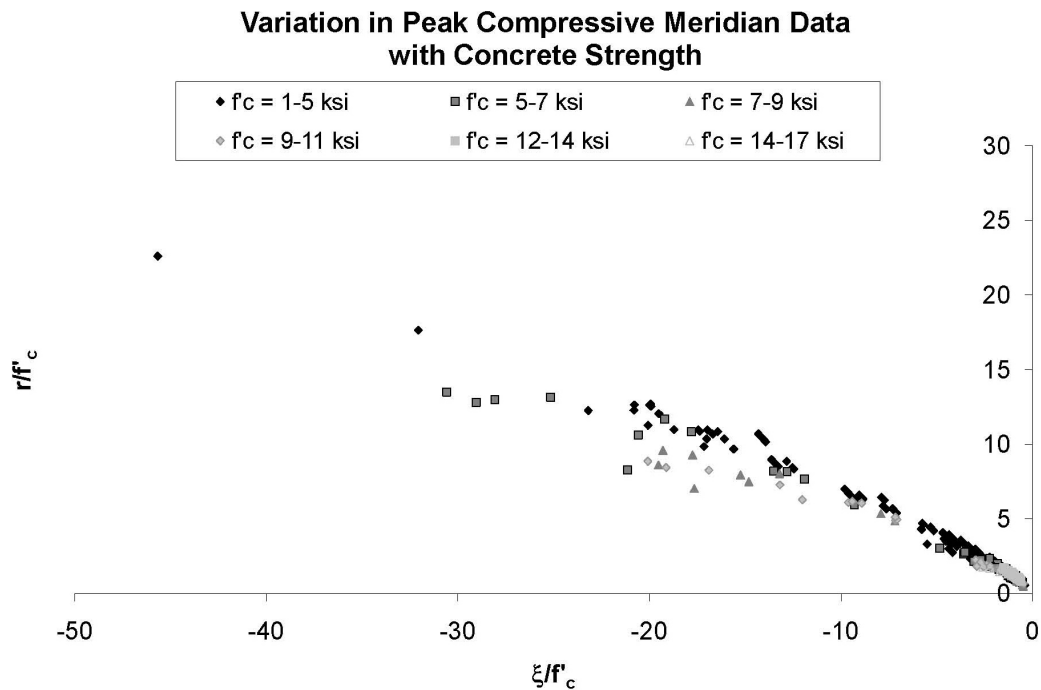


Figure 4.5: Change in the effectiveness of confinement with concrete compressive strength.

uniaxial compressive strength has an influence on the strength increase of concrete due to confinement. Higher strength concretes supposedly do not have as great of an increase in strength with confinement as lower strength concretes. This conclusion is not obvious from the test data compiled for this thesis. For confinement levels with  $\xi/f'_c$  between -2 and 0, the effect of concrete compressive strength is indistinguishable. At higher confinement levels, it becomes possible to observe some effect of the concrete compressive strength. However, the effect of concrete compressive strength is small

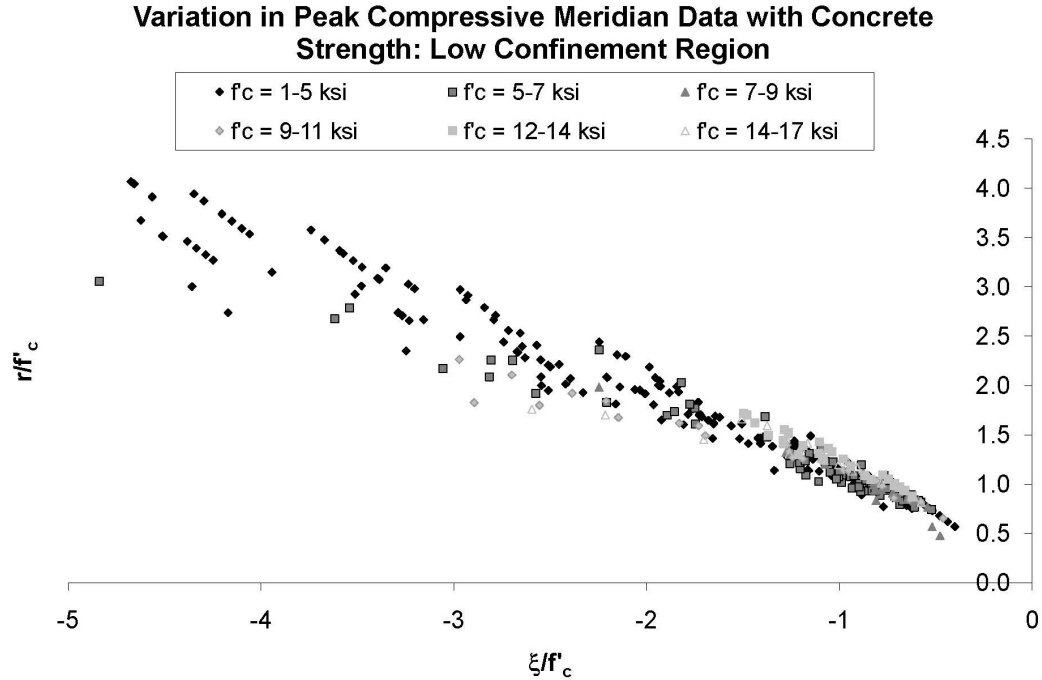


Figure 4.6: Change in the effectiveness of confinement with concrete compressive strength: low confinement region.

relative to the scatter in the data. For this reason, as well as the fact that the intention of this thesis is to model the conditions of passive confinement—which corresponds to the lower confinement range—the change in the effectiveness of confinement with concrete strength was not taken into account in the model presented herein.

Figure 4.7 shows the effect of the type of confinement on the peak compressive meridian data. The only type of tests that yielded results where  $\xi/f'_c$  was less than -5 were tests utilizing a triaxial pressure vessel. Thus, only the lower confinement range is shown for this testing variable. There appears to be a small influence of the testing method that leads to higher strength values in the true triaxial tests than the other testing methods. This topic has been extensively studied elsewhere [for example, Gerstle et al. (1980) and Schickert and Winkler (1977)], and this author will defer to those results as it is outside the scope of this thesis.

Figure 4.8 shows the effect of specimen size on the peak compressive meridian data. All but six of the data points with  $\xi/f'_c$  less than -5 were 6 x 12 inch (152 x 305 mm) cylinders, so the figure is limited to  $\xi/f'_c$  between -5 and 0. The size of the

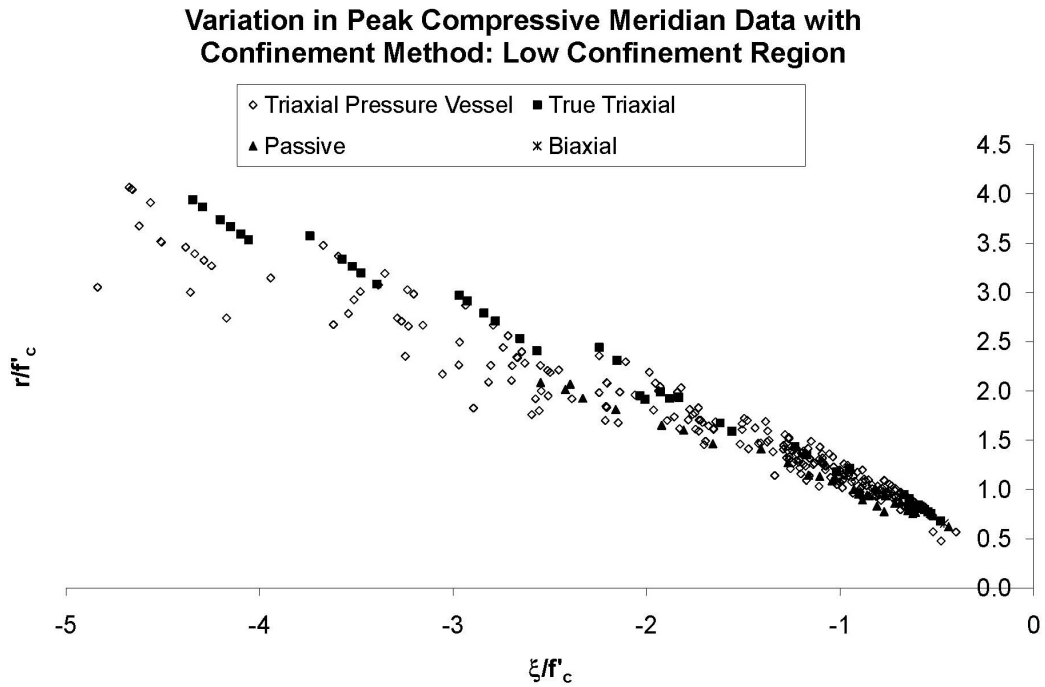


Figure 4.7: Change in the effectiveness of confinement with the confinement method: low confinement region.

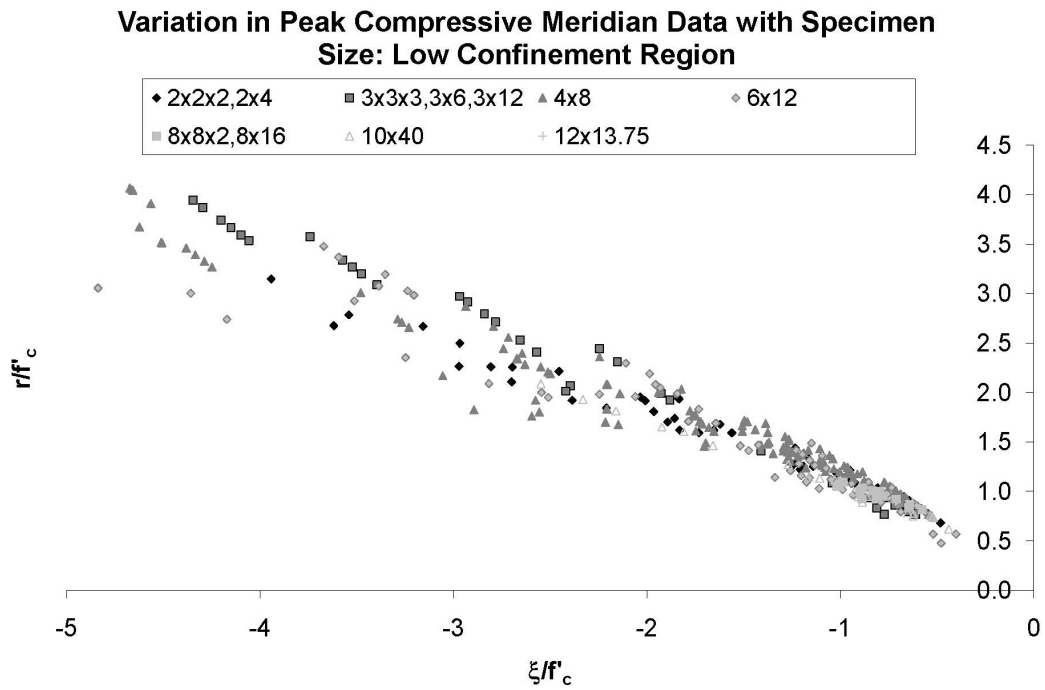


Figure 4.8: Change in the effectiveness of confinement with specimen size: low confinement region.

specimen does not appear to alter the effectiveness of confinement on the strength of the concrete.

An interesting result of bringing this large collection of data together is to consider the generation in which the experiments were performed. Clearly, the technology of concrete testing has advanced considerably from the time of the first published paper in this set of data (Richart et al., 1928). Thus, the data were grouped by the year in which the tests were published in order to determine if this advance in technology has changed the apparent behavior of the concrete. Figures 4.9 and 4.10 show the variation in the results with their year of publication. While the papers published

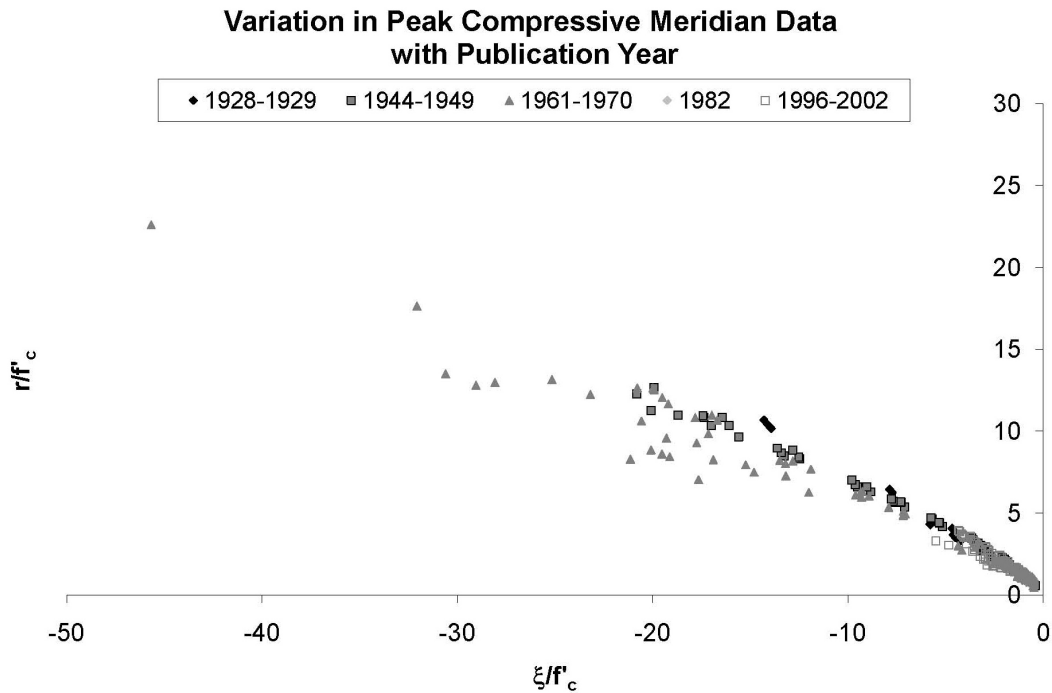


Figure 4.9: Change in the effectiveness of confinement with year of experiment.

from 1961 to 1970 appear to have the largest scatter, there is no distinguishable trend in the data. Thus, it is interesting to note that the now primitive techniques utilized in the 1920s appear to yield quite similar results to tests performed with far more advanced equipment. Regardless, there is clearly no reason to disregard data due to the use of antiquated testing techniques.

Plotting the data in the  $(r, \theta)$  plane requires some data modification due to the fact that the data for a range of Lode angles are never all in the same  $\xi$  plane. Thus,

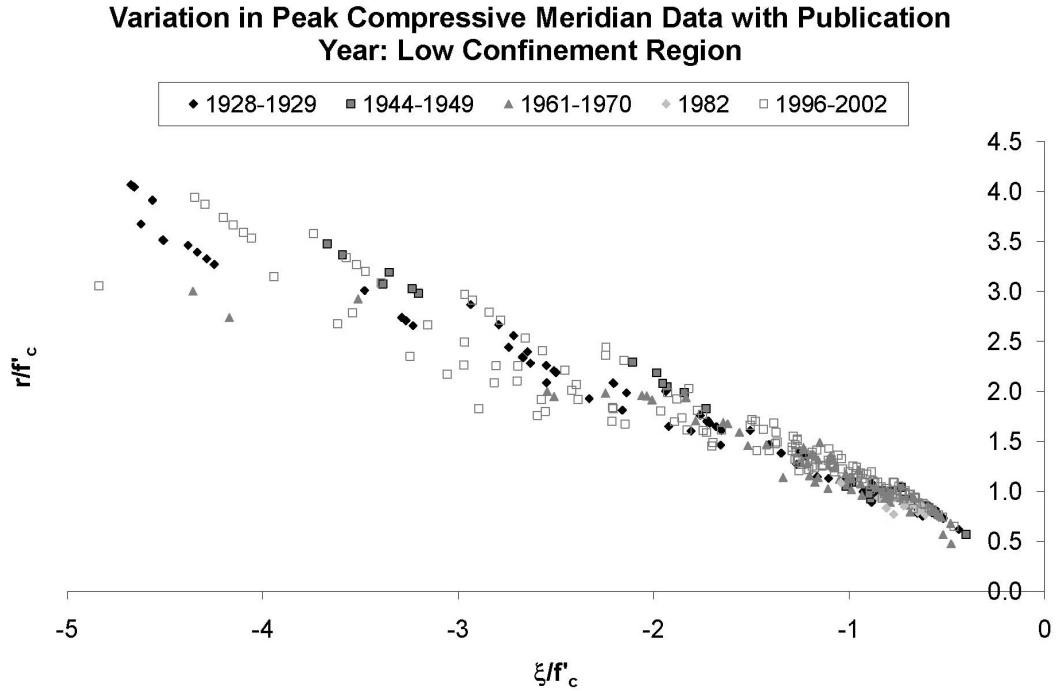


Figure 4.10: Change in the effectiveness of confinement with era of experiment: low confinement region.

to assist in visualizing the shape of the test data, a parabolic fit was performed for  $5^\circ$ - $10^\circ$  increments in the Lode angle, based on the quantity of test data obtained for that Lode angle range. The fit was then evaluated at a specific value for  $\xi$ . In this way, the general shape of the test data can be understood. Figure 4.11 shows the shape of the test data in the  $(r, \theta)$  plane for various levels of  $\xi$ . Recall that values of the Lode angle may only range from  $0^\circ$  to  $60^\circ$ . For the sake of illustration, this range is copied and reflected to the full  $360^\circ$  using the three-fold symmetry of concrete.

### 4.2.3 Peak Surface Fit

As discussed at the beginning of this chapter, the concrete is assumed to be pre-cracked. Thus, two of the parameters for the peak loading surface,  $a_0$  and  $b_0$ , are set to zero. Also, due to the manner in which the loading surface is defined, it is possible to eliminate a third parameter. Consider the unconfined axial loading of a cylindrical specimen. The model must be defined so that the peak surface is reached at a stress state corresponding to the defined compressive strength of the specimen. For this

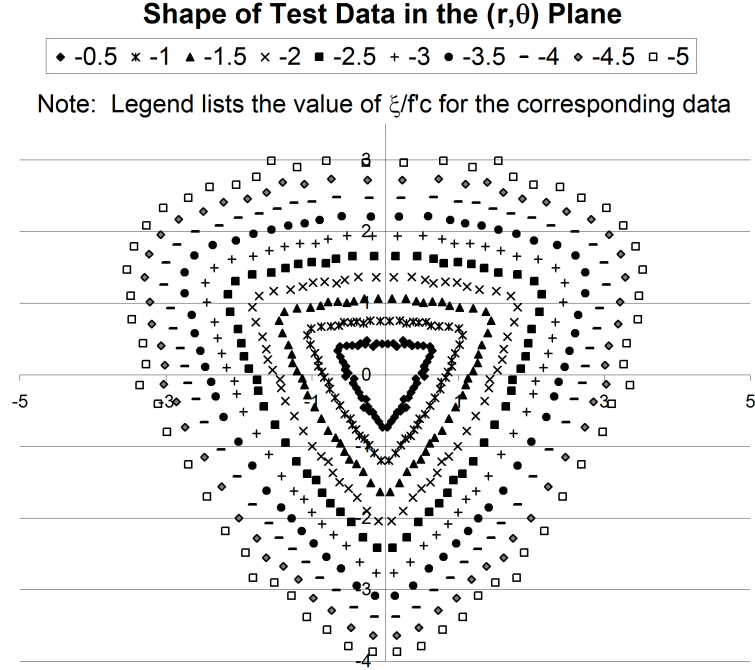


Figure 4.11: Shape of the test data in the  $(r, \theta)$  plane.

case, the triaxial stress state can be defined:

$$\left. \begin{array}{l} \sigma_x = \sigma_y = 0 \\ \sigma_z = -f'_c \end{array} \right\} \text{at uniaxial peak} \quad (4.7)$$

This corresponds to invariant values:

$$\left. \begin{array}{l} \xi = -\frac{f'_c}{\sqrt{3}} \\ r = \sqrt{\frac{2}{3}}f'_c \\ \theta = 60^\circ \end{array} \right\} \text{at uniaxial peak} \quad (4.8)$$

Implementing this stress state into Equation 3.4 for the peak surface gives parameter  $b_1$  in terms of  $b_2$  and  $b_3$ , the remaining compressive meridian parameters:

$$b_1 = \frac{b_2}{\sqrt{3}} - \frac{2}{\sqrt{3}} - b_3 \sqrt{\frac{2}{9}} \quad (4.9)$$

This leaves only five parameters for the peak surface that must be determined using the test data:  $a_1$ ,  $a_2$ ,  $a_3$ ,  $b_2$ , and  $b_3$ .

A least squares fit of the data was performed to estimate the remaining parameters for the peak tensile and compressive meridians. Equation 3.4 defines the peak surface. Since the stress state is on the peak surface when the value of  $F_{peak}$  is zero, the error between each data point and the model is defined using the same equation. Thus, the parameters  $a_1$ ,  $a_2$ ,  $a_3$ ,  $b_2$ , and  $b_3$  for the peak surface were adjusted to minimize the error, defined as:

$$error = \sum_{i=1}^n [r_i - R_{peak}(\xi_i, \theta_i)]^2 \quad (4.10)$$

Using the entire data set, the peak surface parameter values shown in Table 4.1 were obtained. The fit for these parameters is shown with the test data in Figures 4.12

Table 4.1: Peak surface parameters.

Parameter	Value	Parameter	Value
$a_{0,peak}$	0.0	$b_{0,peak}$	0.0
$a_{1,peak}$	-1.3419	$b_{1,peak}$	-3.6425
$a_{2,peak}$	0.1327	$b_{2,peak}$	0.1761
$a_{3,peak}$	0.8889	$b_{3,peak}$	1.8310

and 4.13.

Note that Equation 4.9 requires that the peak compressive meridian pass through the uniaxial peak compression point  $(-\sqrt{\frac{1}{3}}, \sqrt{\frac{2}{3}}) = (-0.58, 0.82)$  in  $(\xi, r)$  space. The scatter in the data near that point is due to the fact that the compressive strength of concrete often varies from specimen to specimen. While the compressive strength of the batch is given at a certain value, different specimens will fail at a different point than defined in Equation 4.8 because of this variation in  $f'_c$ .

It can be seen from the fit that peak compressive meridian data at lower confinement are being somewhat overestimated in this fit. There are only two parameters used to fit the peak compressive meridian:  $b_2$  and  $b_3$ . Thus, it may be the case that the data at higher confinement levels are responsible for the fit being poorer at lower confinement levels. Since the scope of this thesis involves modeling the behavior of passively confined columns, a second fit to the test data was made to obtain better

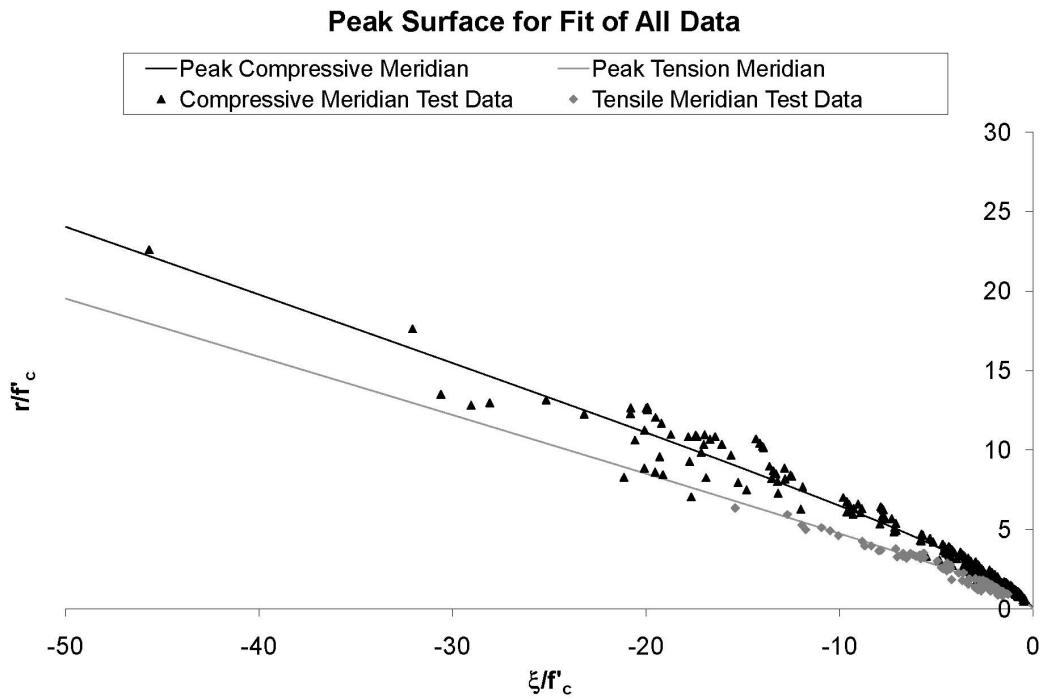


Figure 4.12: Peak compressive and tensile meridians for fit of all data.

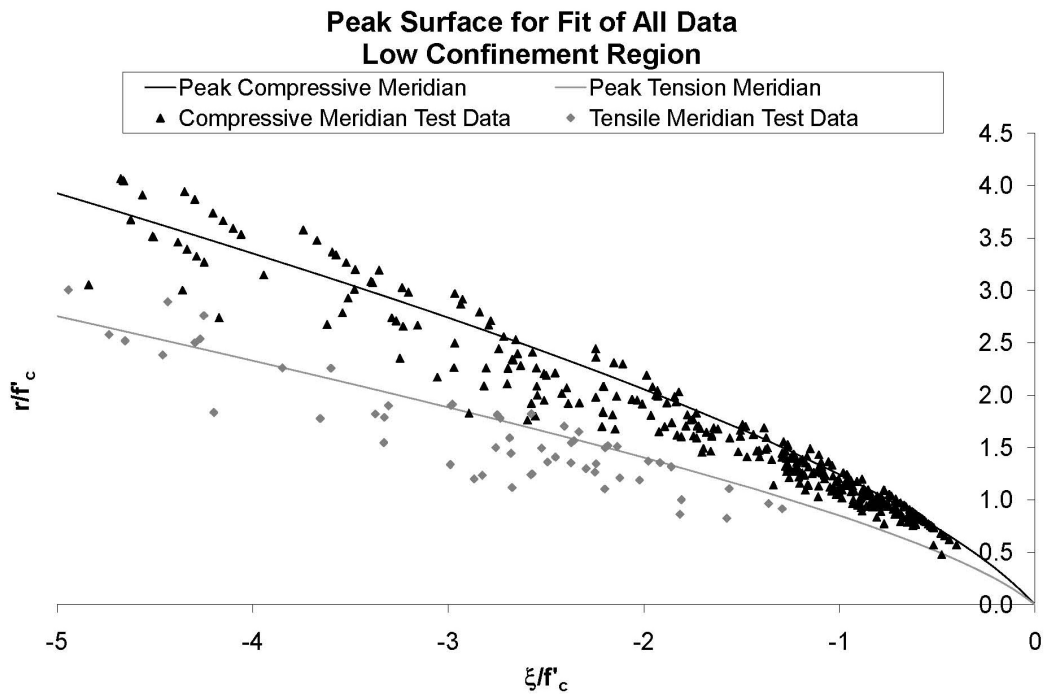


Figure 4.13: Peak compressive and tensile meridians for fit of all data: low confinement region.

correlation in the lower confinement range. However, if the intent is to model the complete triaxial load range of concrete, this first fit represents the best choice of parameters.

For the second fit, the data were limited to the subset having a  $\xi/f'_c$  value between -3.5 and 0.0. This range was chosen as it represents the largest range of values for steel or composite confined columns commonly used for civil engineering applications. All types of loading were used in this fit, not just passive confinement data. The reason for this is due to the physical mechanism being represented. True triaxial loading and triaxial pressure vessels both have a more even stress distribution in the specimen. These testing methods directly measure the lateral stress on the specimen. The passive confinement data uses an assumed formula (given in each individual paper) to calculate an effective lateral stress created by the confinement. However, it is understood that this lateral stress distribution is not evenly distributed over the height of the cylinder due to the fact that the confinement (in the case of steel rebar, for example) is not evenly distributed. Thus, non-passive test data more accurately represent the physical mechanism causing the strength increase through confinement. The finite element model itself will handle the unevenness in the lateral stress distribution. For this reason, the entire set of data for low confinement was utilized for this second fit.

Parameter estimates resulting from the second fit are defined in Table 4.2. These values for the parameters were used to validate the model (Chapter 6) and predict concrete behavior (Chapter 7). A comparison of the peak tensile and compressive

Table 4.2: Peak surface parameters for low confinement range.

Parameter	Value	Parameter	Value
$a_{0,peak}$	0.0	$b_{0,peak}$	0.0
$a_{1,peak}$	-1.4344	$b_{1,peak}$	-1.9711
$a_{2,peak}$	0.0924	$b_{2,peak}$	0.3103
$a_{3,peak}$	1.1005	$b_{3,peak}$	0.7039

meridians for both fits is shown in Figures 4.14 and 4.15. The second fit reduces the overestimation of the data in the low confinement range. However, the peak

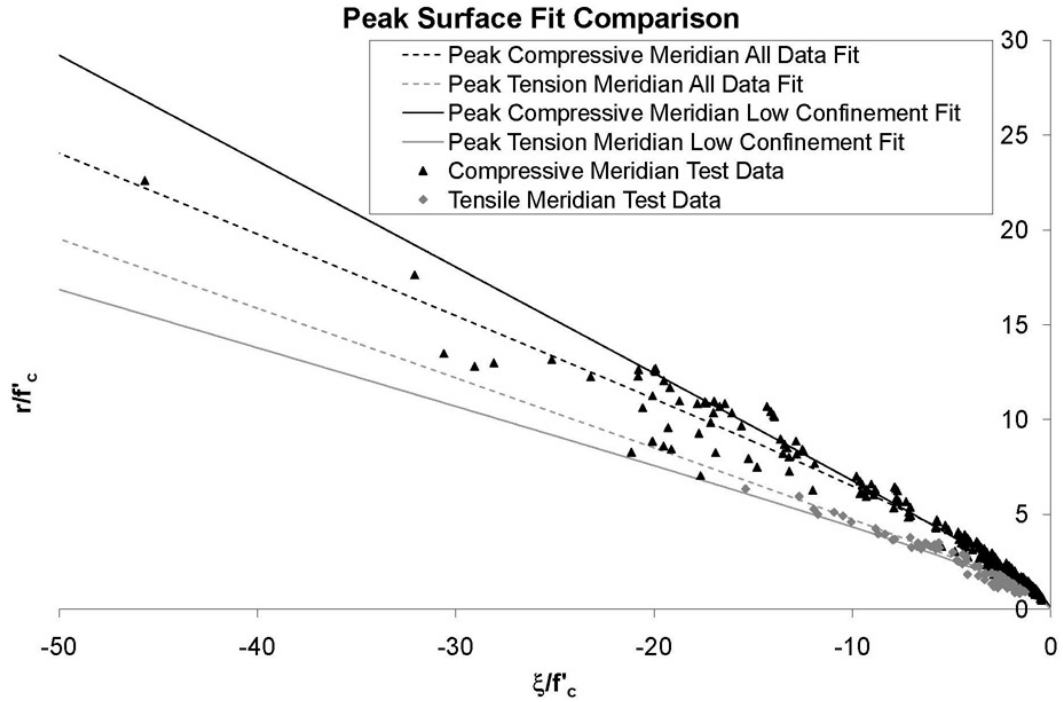


Figure 4.14: Comparison of peak compressive and tensile meridians for two different fits.

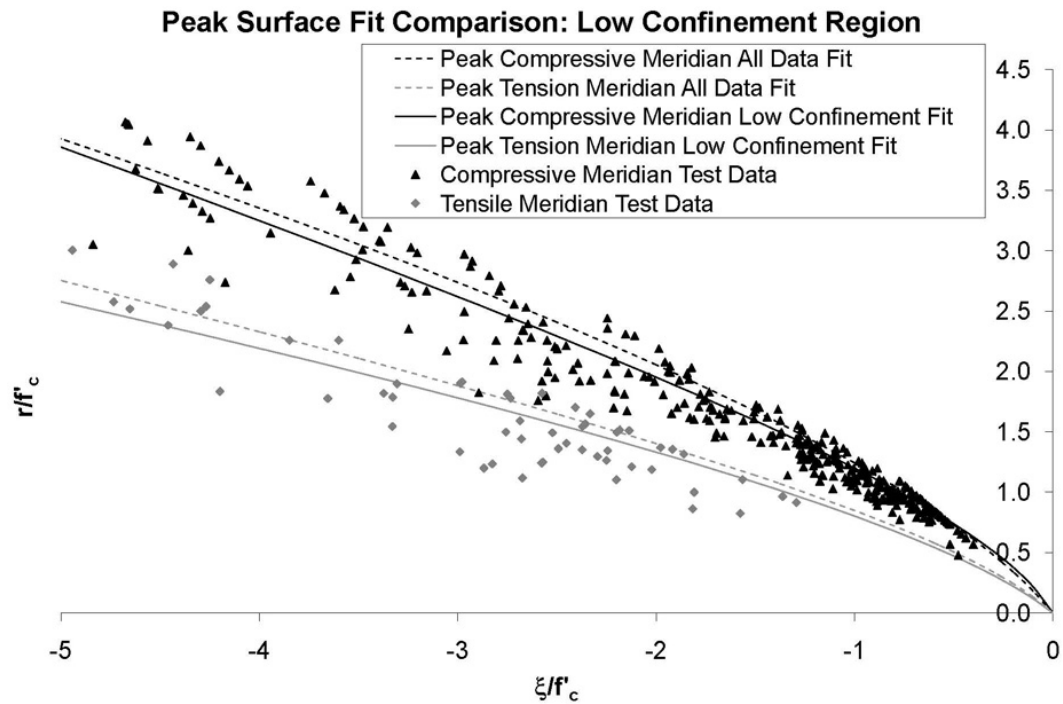


Figure 4.15: Comparison of peak compressive and tensile meridians for two different fits: low confinement region.

compressive meridian still does not lie near the middle of the data. One reason is the requirement that the peak compressive meridian pass through the uniaxial peak point  $(-0.58, 0.82)$  as previously discussed. This is, however, a valid requirement to enforce. Also, the model assumed a hyperbolic shape of the meridian with only two remaining parameters to fit to the data. However, the fact that the peak compressive meridian does not pass through the middle of the data is not considered a problem for this case. As discussed in Section 4.2.2, peak compressive meridian data points that lie close to, or within, the peak tensile meridian data points are clearly suspect since they may be due to problems with the test setup. For these reasons, a slight overestimation of the peak compressive meridian data is considered acceptable.

The peak compressive meridians for the two different fits are compared to two existing models in Figures 4.16 and 4.17. One of the two existing models is discussed in Malvar et al. (1994) and Malvar et al. (1996) and the other in ANATECH Corp. (1998). It is clear that a hyperbola represents the better fit to data when considering both high and low confinement ranges. Although a separate fit was utilized in this thesis to better fit the lower confinement range, a hyperbolic shape is still a superior choice to the two models shown.

### 4.3 Residual Surface Correlation

Papers showing the full stress versus strain behavior of multiaxially loaded concrete are somewhat rare. Few papers extend to a large enough strain to be useable in determining the residual stress of the concrete. Thus, only five sets of experiments were found to determine the parameters defining the residual surface. Test data from Ansari and Li (1998), Attard and Setunge (1994), and Attard and Setunge (1996), used for the peak surface, were also able to be utilized for determining the residual surface parameters. Details of those papers are discussed in Section 4.2.1.1. An additional three data sets were obtained from Jamet et al. (1984), van Mier (1984), and Xie et al. (1995) to be used in determining the residual surface parameters. These three papers will be discussed in Section 4.3.1. The compilation of the residual

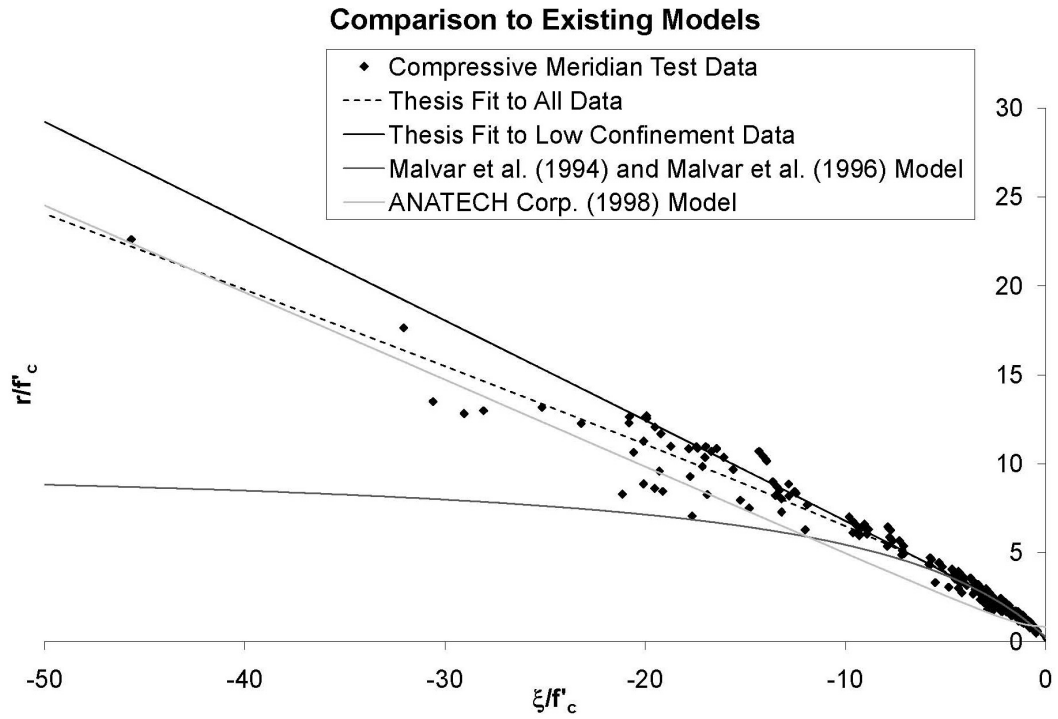


Figure 4.16: Comparison of peak compressive meridian to existing models.

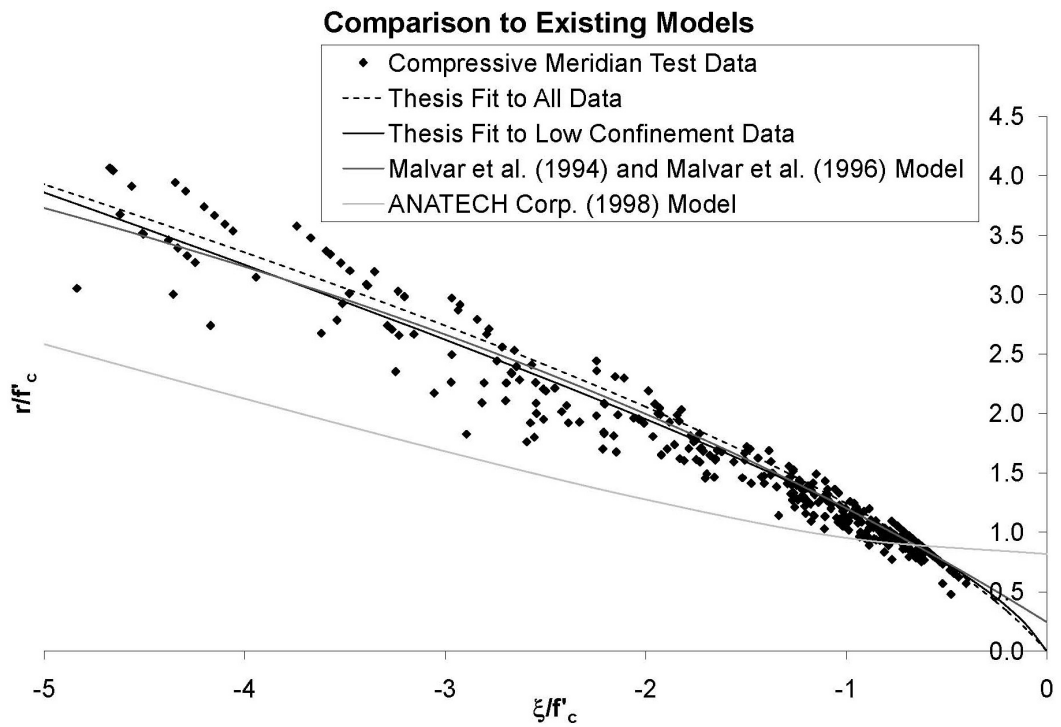


Figure 4.17: Comparison of peak compressive meridian to existing models: low confinement region.

surface data is shown and discussed in Section 4.3.2. Last, the method for choosing the parameters defining the residual surface is discussed in Section 4.3.3.

### 4.3.1 Residual Surface Papers

Four of the five experiments used a triaxial pressure vessel as previously described in Section 4.2.1. The fifth used a true triaxial setup, also described in Section 4.2.1. Thus, only one of these experiments had test data for a Lode angle other than  $60^\circ$ . However, a fairly large range of some important variables was obtained in the limited number of papers found. Concrete compressive strengths from 4.2 to 19.1 ksi (29 to 132 MPa) were tested. Cylinder sizes from 2.19 x 4.33 inches (55.5 x 110 mm) to 4 x 8 inches (100 x 200 mm) and cubes of 4 x 4 x 4 inches (100 x 100 x 100 mm) were all considered in the tests. While the variable range was not nearly as great as that of the peak surface data, a reasonable amount of variation in the testing variables was seen in the five sets utilized for the residual surface. A summary of these five sets of test data can be found in Table D.1.

Jamet et al. (1984) performed a limited set of experiments up to strain levels of 10%, with the focus on measuring the axial and lateral deformation patterns. One mix of normal strength concrete, with a water-cement ratio of 0.53, was used to create the specimens. The final concrete compressive strength of the 4.33 x 8.66 inch (110 x 220 mm) cylinders was 4.2 ksi (29 MPa). Specimens were sealed and stored in the molds for 48 hours, then removed and stored for 30 days at 65% relative humidity. At this point, some amount of grinding was performed to ensure true parallelism between all faces. Finally, the cylinders were again stored at 65% relative humidity for 180 more days before being removed for testing. A triaxial pressure vessel was utilized to apply confining pressures of 0.4, 1.5, 3.6, 7.3, and 14.5 ksi (3, 10, 25, 50, and 100 MPa). Unfortunately, tests employing confining pressures of 7.3 and 14.5 ksi (50 and 100 MPa) were terminated before the residual stress was reached and so could not be used for determining the residual surface parameters. During testing, the cylinders were jacketed in rubber sleeves to prevent penetration of the confining

fluid. Specimens were first loaded hydrostatically until the desired confining pressure was reached. The axial load was then increased to a total axial strain of 10%. The authors concluded that, as confining pressures are increased, concrete transitions from drastic strain softening behavior to that of classical ductility. It was also determined that the lateral strains achieved by the cylinders were strongly dependent upon the magnitude of the confining pressure.

van Mier (1984) studied the strain softening behavior of concrete under multiaxial loading conditions. A triaxial testing machine was constructed for this purpose. Details of this machine can be found in the cited paper. The machine allowed for independent loading of the specimens in three orthogonal directions. One mix of concrete with a water-cement ratio of 0.50 was used to create all of the 4 inch (100 mm) cubes. Specimens were cast in 28 x 5 x 5 inch (700 x 135 x 135 mm) prisms. The prisms were stored under water for 28 days and then removed and cut into 4.1 inch (104 mm) cubes. These cubes were then ground flat to the desired size to ensure that all faces were parallel. The final specimens were then stored in plastic bags at room temperature until testing. The age at testing ranged from 71 to 252 days, leading to a range of concrete compressive strengths of 5.8 to 7.4 ksi (39.9 to 51.0 MPa). Specimens were tested in a variety of loading paths: uniaxial, biaxial, triaxial, constant stress-ratio, constant strain-ratio, etc. The author found that the casting direction of the concrete had a significant effect on the ductility of the specimen under uniaxial loading. Casting direction refers to whether the axially loaded direction was horizontal or vertical when the specimen was originally cast. Two different failure mechanisms were observed for Lode angles near  $60^\circ$  and near  $0^\circ$ . For Lode angles near  $60^\circ$ , corresponding to the compressive meridian, fracture occurred in a large number of inclined planes. This type of failure corresponded to a more ductile strain softening behavior. Lode angles near  $0^\circ$ , corresponding to the tensile meridian, showed a planar fracture with failure occurring mainly in one direction. This type of failure showed a more brittle strain softening behavior. The author noted that failure along the compressive meridian showed a significant increase in ductility with confining pressure, while failures along the tensile meridian were not as significantly influenced

by an increase in confining pressure.

Xie et al. (1995) studied the triaxial behavior of high strength concretes. Three different concrete mixes were used with water-cement ratios of 0.321, 0.283, and 0.216 for compressive strengths at testing of 8.7, 13.4, and 17.3 ksi (60.2, 92.2, and 119 MPa) which were tested at 29, 35, and 39 days, respectively. The 2.19 x 4.33 inch (55.5 x 110 mm) cylinders were encased in a polyurethane membrane for testing in a modified Hoek cell. Eleven different confining pressures were tested for each concrete strength ranging from  $0.01f'_c$  to  $0.50f'_c$ . The authors concluded that high strength concrete is less ductile than normal strength concrete. However, like normal strength, increasing confinement leads to an increase in the maximum and residual compressive strengths and improves the ductility.

### 4.3.2 Residual Surface Data

Similar to the yield stress, the residual stress is a somewhat ambiguous quantity. Following the definition laid out in Xie et al. (1995), the residual stress was defined as the point at which the magnitude of the descending slope of the stress-strain curve is less than 2% of the initial elastic slope of the curve. This definition resulted in much of the test data being thrown out. Specifically, all data for Lode angles other than  $60^\circ$  (found only in van Mier (1984)) did not meet this requirement. Figure 4.18 shows the remaining test data, all of which lie on the compressive meridian. It is difficult to see the effect of different variables with such a small set of data. It is interesting to note that the data from van Mier (1984), Ansari and Li (1998), and Jamet et al. (1984) appear to lie on the same curve, while Xie et al. (1995), Attard and Setunge (1994), and Attard and Setunge (1996) appear to lie on a different curve. There is nothing obvious to differentiate these two sets of experimental data that would lead to a different behavior from each other. It is clear that more testing is necessary to determine the effect of different variables on the residual stress of concrete.

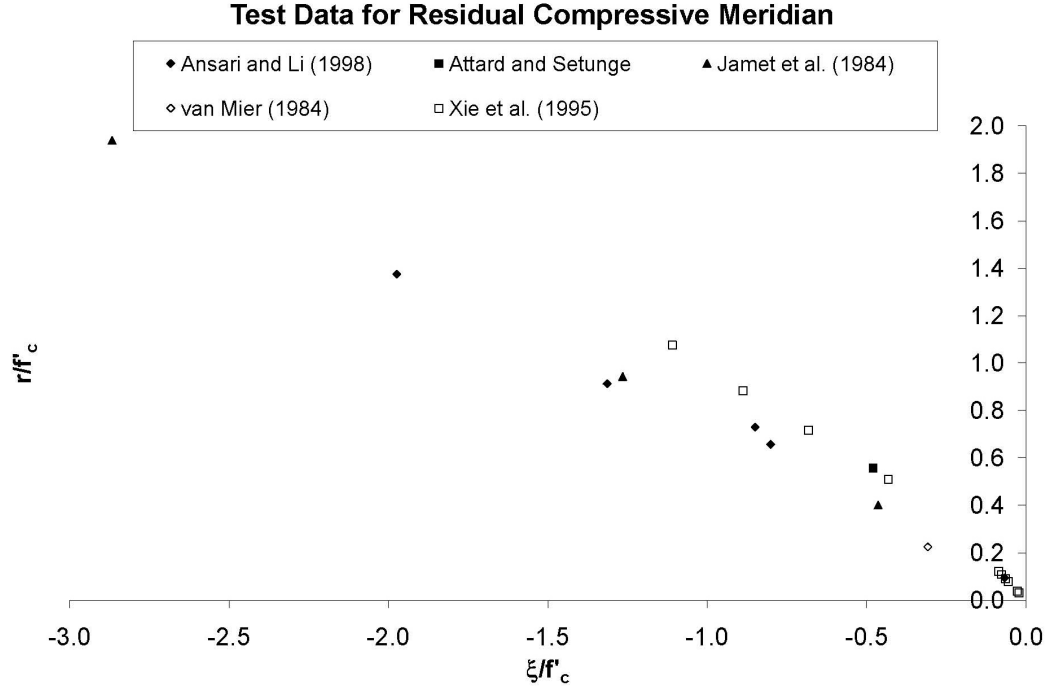


Figure 4.18: Test data for residual compressive meridian.

### 4.3.3 Residual Surface Fit

As discussed at the beginning of this chapter, due to the concrete being defined as pre-cracked, parameters  $a_0$  and  $b_0$  for the residual surface are set to zero. Due to lack of data for Lode angles other than  $60^\circ$ , the ratios of the tensile meridian parameters to the compressive meridian parameters for the residual surface were set equal to that of the peak surface. Thus, it was only necessary to determine the parameters for the compressive meridian.

The parameters defining the compressive meridian of the residual surface were determined by performing a least squares fit to the previously discussed test data. Similar to Equation 4.10, the least squares error minimized for the residual compressive meridian is defined by:

$$error = \sum_{i=1}^n [r_i - r_{c,residual}]^2 \quad (4.11)$$

The definition of  $r_{c,residual}$  is given by Equation 3.1.

Determining the parameters using only this fit created a residual surface that intersects the uniaxial load path in the  $(\xi, r)$  space at two locations, as shown in Figure 4.19. This is physically incorrect. Under uniaxial loading, the specimen will

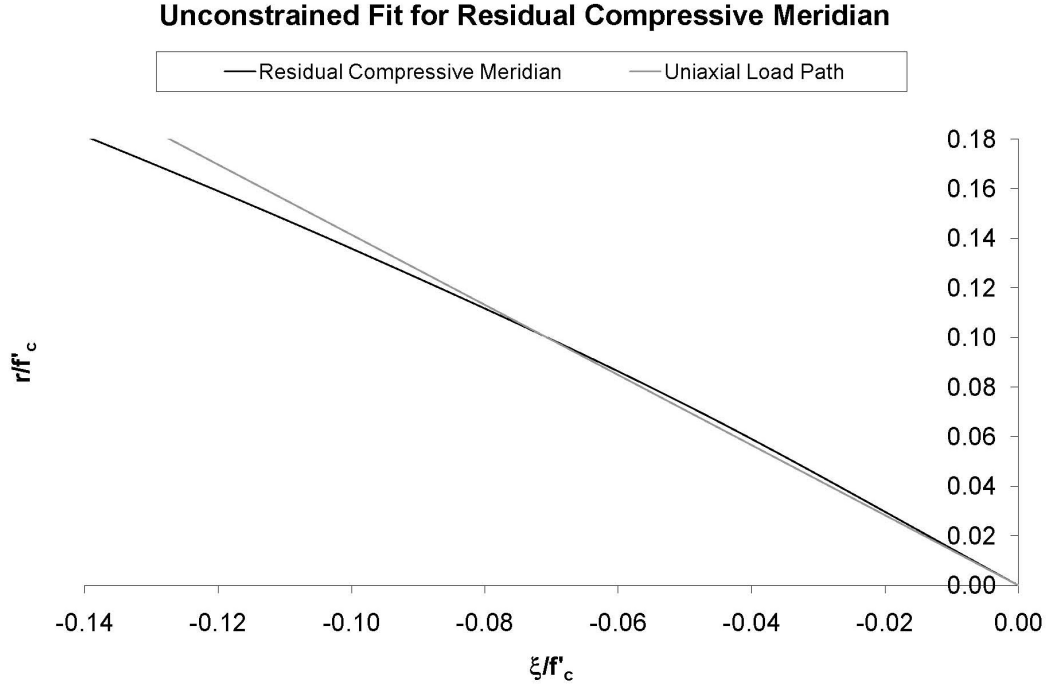


Figure 4.19: Fit for residual compressive meridian with no constraints on the parameters.

soften until the load path intersects the residual surface. For this loading case, it should be possible for the specimen to soften down to a zero stress state. However, the model is defined such that the stress state stops changing when the residual surface is reached. Thus, the residual surface must only intersect the uniaxial load path at the origin. Therefore, it was necessary to introduce a constraint that the slope of the residual surface be tangent to the uniaxial load path at the origin of the  $(\xi, r)$  space. From Equation 4.8, it can be seen that the slope of the uniaxial load path (which is a line in  $(\xi, r)$  space) is:

$$r = -\xi\sqrt{2} \quad (4.12)$$

By taking the derivative of Equation 3.1 and setting the derivative equal to  $-\sqrt{2}$  at

$\xi = 0$ , we can eliminate the parameter  $b_3$ .

$$b_3 = -\frac{b_1}{\sqrt{2}} \quad (4.13)$$

Using this constraint, the parameters defining the residual compressive meridian were determined through a least squares fit. With the ratio of the tensile to compressive meridian parameters determined by the peak surface parameters given in Table 4.2, the parameters for the tensile meridian of the residual surface were calculated. The

Table 4.3: Residual surface parameters.

Parameter	Value	Parameter	Value
$a_{0,residual}$	0.0	$b_{0,residual}$	0.0
$a_{1,residual}$	-0.9764	$b_{1,residual}$	-1.3417
$a_{2,residual}$	0.0565	$b_{2,residual}$	0.1898
$a_{3,residual}$	1.4833	$b_{3,residual}$	0.9847

values for the parameters, defined in Table 4.3, were used to validate the model (Chapter 6) and predict concrete behavior (Chapter 7). The compressive meridian for the residual surface is shown along with the test data in Figure 4.20.

## 4.4 Determination of the Equation for the Damage Increment

The intent of this thesis is to model the increase in the strength and ductility of concrete due to confinement. The effect on strength is handled by the shape of the loading surfaces discussed in Sections 4.1, 4.2, and 4.3. The variable that affects ductility in the model is the damage parameter,  $\psi$ . The damage parameter defines the location of the failure surface as a function of the strain state. However, the damage parameter is simply the sum of the damage increments,  $d\psi$ , over the load path. Thus, ductility will be controlled by the definition of the damage increment,  $d\psi$ .

The magnitude of the damage increment,  $d\psi$ , (for a given load increment) as a

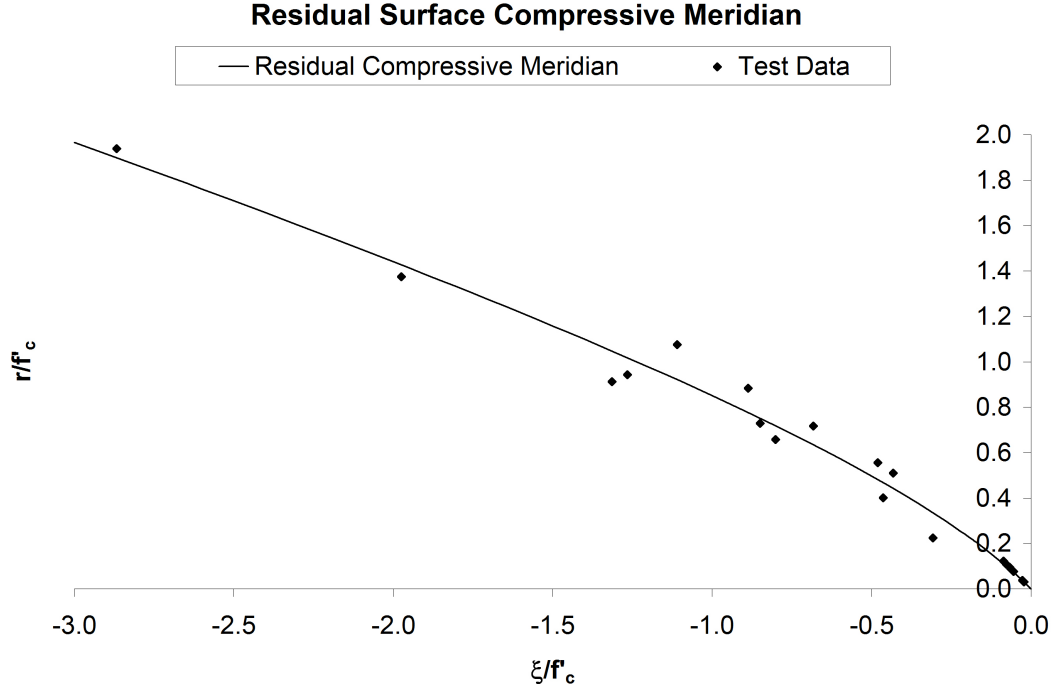


Figure 4.20: Final fit for the residual surface compressive meridian.

function of confinement, accounts for the increase in ductility due to confinement. The invariant  $\xi$ , defined in Equation 2.10, is representative of the amount of confinement present in the material, as it is a measure of the hydrostatic state of stress. Therefore, it is desirable to determine the nature of the relationship between the increment in damage,  $d\psi$ , and the invariant  $\xi$ .

The functional relationship between  $\xi$  and  $d\psi$  cannot be seen directly from test data. Since the damage level is an artificially created quantity, it cannot be measured by concrete testing. Thus, it is necessary to find a state where the damage level is a known value and a related, measurable quantity is also at a known value. This occurs at the peak stress of the concrete. At the peak stress, as previously defined in Equation 3.8,  $\psi$  is equal to  $\psi_{peak}$ , and the strain at peak stress,  $\epsilon_{peak}$ , can be easily determined from the test data. It is also necessary that  $\psi_{peak}$  and  $\epsilon_{peak}$  be related if the assumption is to be made that they vary with  $\xi$  in a similar way. The model has been defined (following traditional plasticity theory) such that the increment in damage,  $d\psi$ , is directly proportional to the normalized plastic strain increment,  $\overline{d\epsilon_p}$  (through a relationship that involves  $\xi$ , see Equation 3.5). Thus,  $d\psi$  is going to be a

function of the strain at peak stress, since  $\epsilon_{peak}$  contributes to  $\overline{d\epsilon_p}$ . A variable that affects  $\epsilon_{peak}$  will affect  $d\psi$  in the same way. Therefore, to determine the relationship between the damage increment and the stress invariant  $\xi$ , the variation of  $\epsilon_{peak}$  will be examined for different confinement levels and concrete compressive strengths. The functional form of the relationship between  $d\psi$  and  $\xi$  is chosen as the same form between  $\epsilon_{peak}$  and  $\xi$ .

The relationship between the damage increment,  $d\psi$ , and the plastic strain increment,  $d\epsilon_{ij}^p$ , will be determined by observing the relationship between the strain at peak stress and the confinement level. Data from Attard and Setunge (1994), Attard and Setunge (1996), Candappa et al. (1999), Candappa et al. (2001), Smith et al. (1989), and Xie et al. (1995) were utilized to explore this relationship. All of the data were used for previous parameter determination except Smith et al. (1989). Discussion of the other papers can be found in Sections 4.2.1.1 and 4.3.1. Details of the experiments performed by Smith et al. (1989) will be discussed in Section 4.4.1. This collection of data will be explored in Section 4.4.2, and the final relationship for  $d\psi$  and determination for the value of  $\gamma$  will also be discussed.

#### 4.4.1 Papers Used to Determine the Equation for the Damage Increment

Details of the experiments from Attard and Setunge (1994), Attard and Setunge (1996), Candappa et al. (1999), and Candappa et al. (2001) are discussed in Section 4.2.1.1. Discussion of the experiments performed in Xie et al. (1995) is in Section 4.3.1.

Smith et al. (1989) performed a set of experiments to determine the post-peak behavior of concrete under triaxial loading. A triaxial pressure vessel was used to apply lateral confinement to the 2.125 x 4.250 inch (54 x 108 mm) cylinders. The specimens were encased in a polyurethane membrane during testing. One mix of concrete was created to cast thirty-five of the specimens. A water-cement ratio of 0.83 was used for a final compressive strength of 5.0 ksi (34.5 MPa). Blocks of concrete

6 x 6 x 10 inch (152 x 152 x 254 mm) were cast and aged for eight months. At that time, the blocks were removed and the cylinders cored out and used for testing. An additional sixteen specimens were furnished by the Waterways Experiment Station that had a final compressive strength of 6.4 ksi (44.1 MPa). However, the results from the testing of these specimens were not used in this thesis for the determination of failure surface and flow rule parameters due to the fact that they were cyclically loaded. The 5.0 ksi (34.5 MPa) specimens were loaded laterally up to the desired confining pressure. The axial load was then increased to an axial strain level of 5%. The authors concluded that increasing confining pressure leads to a transition from brittle to ductile post-peak behavior. They further concluded that the plastic strain increments at peak were not compatible with an associated flow rule. The volume dilatation was somewhat less than an associated flow rule would predict. Last, the general stress versus strain behavior of different strength concretes is similar, but with a trend of increasing brittleness with increasing strength.

#### **4.4.2 Discussion of Test Data Used to Determine the Equation for the Damage Increment**

Several authors noted that the change in ductility with confinement is different for normal- versus high-strength concrete. This was discussed in Sections 4.2.1, 4.3.1, and 4.4.1. Therefore, the effect of the concrete compressive strength on the axial strain at peak stress must also be explored if its effect is to be taken into account in the model. It is necessary to understand how both the concrete compressive strength and the confinement level change the strain at peak stress.

The way in which the concrete compressive strength changes the behavior of the strain at peak stress is examined by considering the unconfined loading case. Figure 4.21 shows the axial strain at peak unconfined stress plotted against the concrete compressive strength. No correlation appears between these two quantities. Thus, it is assumed that the concrete compressive strength only affects how confinement changes the strain at peak stress, but it does not directly affect the strain at peak

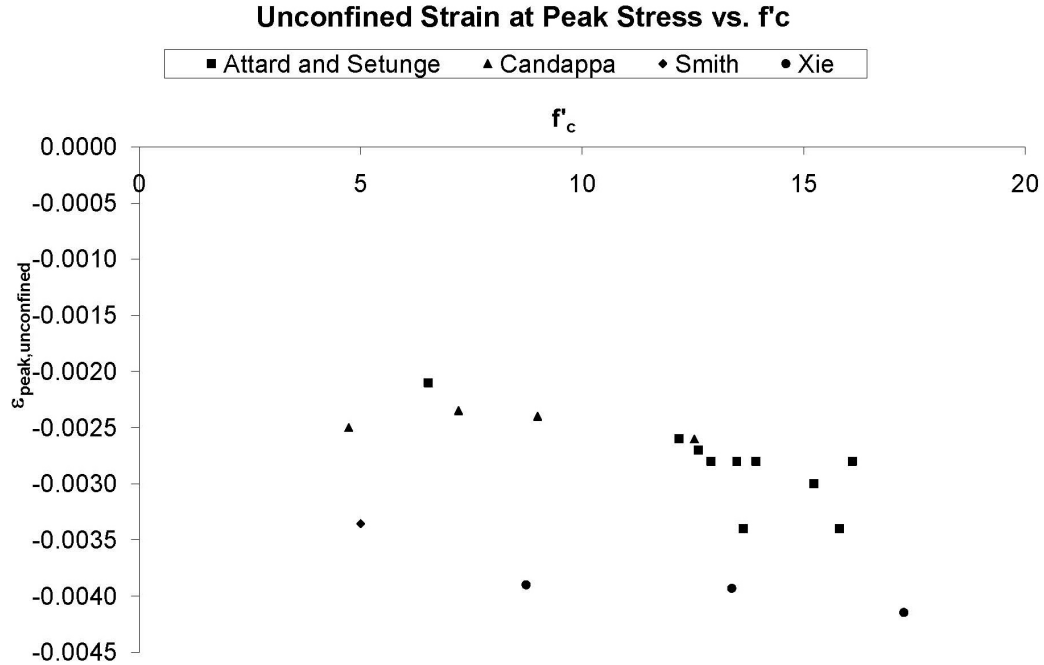


Figure 4.21: Variation of strain at unconfined peak stress with concrete compressive strength,  $f'_c$ .

stress itself. In order to examine this effect, it is necessary to explore the *change* in strain at peak confined stress for various confinement levels and concrete compressive strength.

It is clear from Figure 4.21 that different concretes have a different strain at unconfined peak stress. To study only the change in strain at peak stress with confinement, the ratio of the strain at peak stress for the confined case to the strain at peak stress for the unconfined case is observed. This allows the variation in the unconfined strain at peak stress to be normalized out of the behavior.

Figure 4.22 shows the ratio of the confined to unconfined strain at peak stress plotted against the invariant  $\xi$ . It can be seen that a roughly linear relationship between the strain ratio and  $\xi$  exists. The slope of this line appears to vary with the compressive strength of the concrete.

Malvar et al. (1994) proposed that the relationship between the damage parameter

### Variation of Strain at Peak Stress with Confinement and Concrete Strength

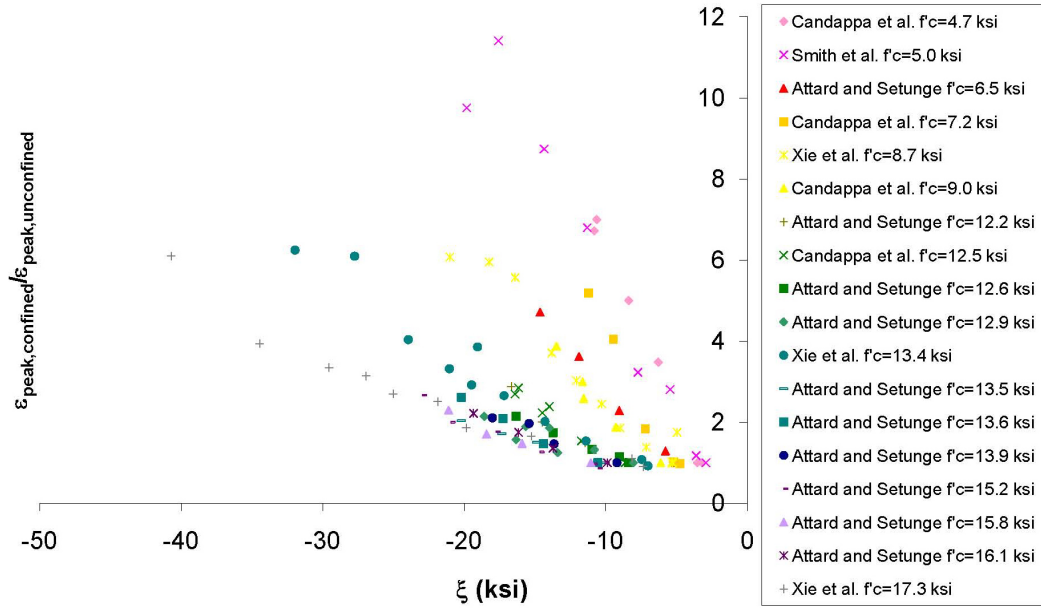


Figure 4.22: Ratio of confined strain to unconfined strain at peak stress plotted versus  $\xi$ .

and confinement be defined by:

$$d\psi = \frac{\overline{d\epsilon^p}}{r_f \left(1 + \left|\frac{p}{f_t}\right|\right)^b} \quad (4.14)$$

The form of this equation was used as a starting point for the relationship for  $d\psi$ . The parameters  $r_f$  and  $b$  were to be estimated for their model. This thesis replaces the quantity represented by the hydrostatic pressure,  $p$ , with the invariant  $\xi$ . Further, the tension strength of concrete,  $f_t$ , is known to vary as the square root of the concrete compressive strength  $f'_c$  (Nilson, 1997). Thus, it is implied that by normalizing the invariant  $\xi$  with the square root of the concrete compressive strength, the variation with  $f'_c$  should disappear.

Figure 4.23 shows the ratio of confined to unconfined strain at peak stress plotted against the ratio of  $\xi$  to the square root of the concrete compressive strength. Scatter still exists within the data due to the concrete compressive strength. Thus, this relationship is not adequate to determine how the peak strain should vary with both

**Variation of Strain at Peak Stress as Proposed  
by Malvar et al. (1994)**

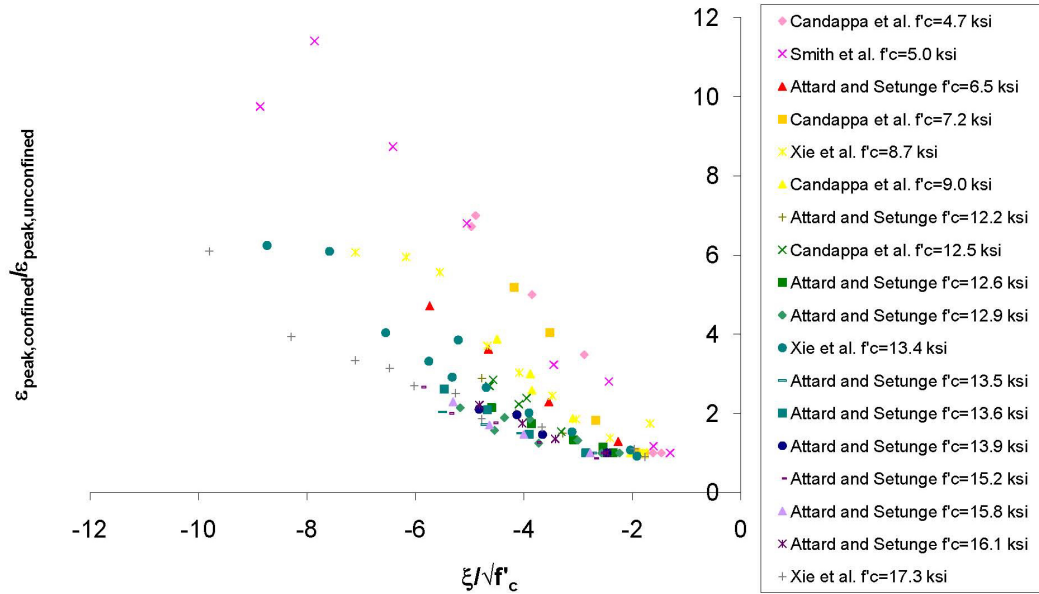


Figure 4.23: Ratio of confined strain to unconfined strain at peak stress plotted versus  $\xi/\sqrt{f'_c}$ .

the invariant  $\xi$  and  $f'_c$ .

The equations for the loading surfaces of this model predict that the shape of the surface will scale with the ratio of  $\xi$  to the concrete compressive strength itself. Further, the linear relationship shown in Figure 4.22, with only the slope of the line varying with  $f'_c$ , implies that the increase in strain at peak stress should scale with  $\xi/f'_c$ . Thus, the ratio of confined to unconfined strain at peak stress was plotted against the ratio of  $\xi$  to the concrete compressive strength in Figure 4.24. While scatter still exists in the data, there is no longer a distinguishable trend in this scatter based on the concrete compressive strength. Thus, it is defined that the damage level will vary with the ratio of  $\xi$  to  $f'_c$ .

By comparing Figure 4.22 to Figure 4.24, the behavior no longer appears linear. A power law was chosen to represent this relationship. A least squares fit of the power law is shown with the data in Figure 4.25. The Smith et al. (1989) data point plotted at the extreme left of all the data points may appear to call into question the validity of the power law fit. However, examining this data point relative to the others in

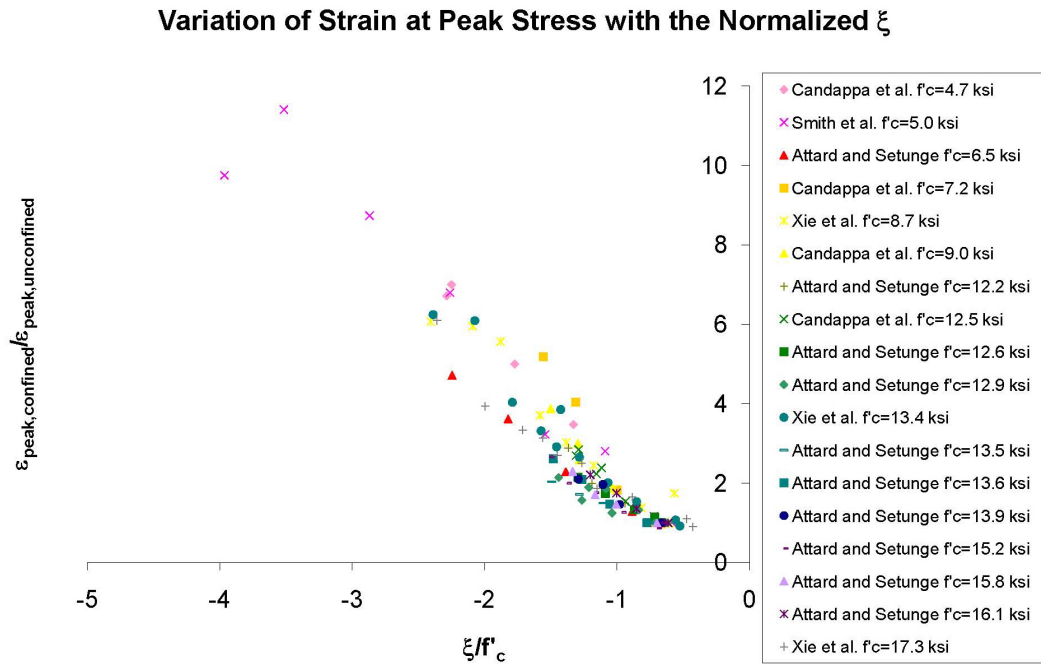


Figure 4.24: Ratio of confined strain to unconfined strain at peak stress plotted versus  $\xi/f'_c$ .

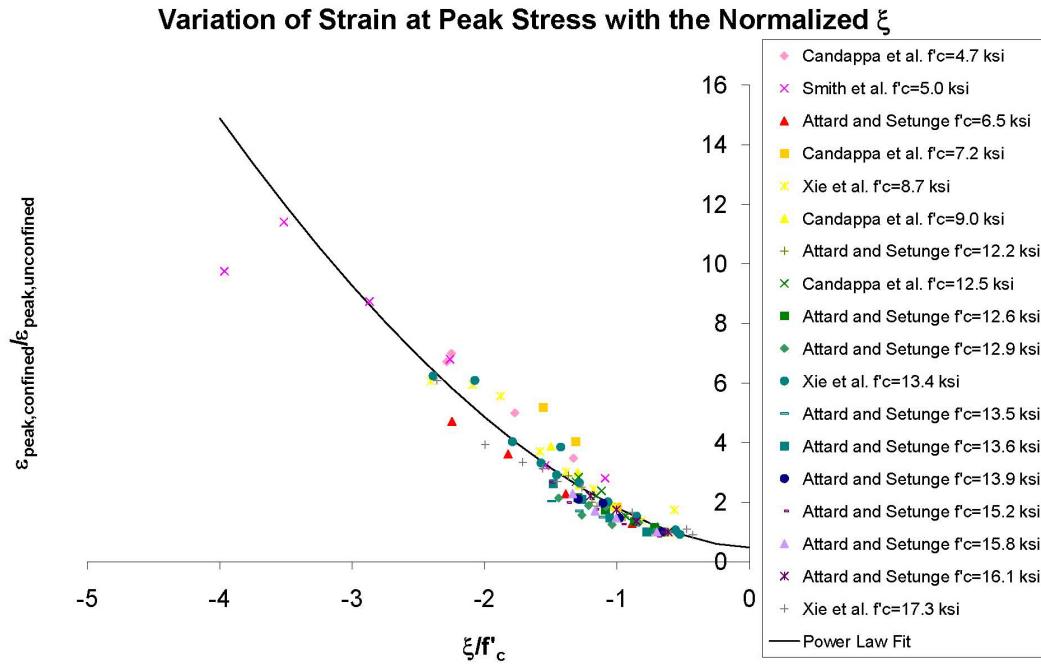


Figure 4.25: Power law fit for ratio of confined strain to unconfined strain at peak stress versus  $\xi/f'_c$ .

his experiments, it very quickly becomes apparent that this is an anomalously low value for the strain at peak stress. Consider the raw data for the eight data points from Smith et al. (1989) shown in Table 4.4. From the trend in the  $\epsilon_{peak}$  values, it is

Table 4.4: Smith et al. (1989) raw data points.

$\sigma_{confining}$ (ksi)	$\sigma_{peak}$ (ksi)	$\epsilon_{peak}$
0.0	-5.0	-0.003
-0.1	-6.0	-0.004
-0.5	-8.4	-0.009
-1.0	-11.4	-0.011
-2.0	-15.6	-0.023
-3.0	-18.8	-0.029
-4.0	-22.4	-0.038
-5.0	-24.3	-0.033

expected that the strain at peak stress for the final load point would be near -0.047, which corresponds to a ratio of confined to unconfined strain at peak stress of 15.7. The power law fit predicts a ratio of 14.7. Thus, while this data point appears to call into question the power law fit, it can be disregarded.

The equation describing the power law as fit to the data is given by:

$$\frac{\epsilon_{peak,confined}}{\epsilon_{peak,unconfined}} = 1.3276 \left( \frac{|\xi|}{f'_c} \right)^{1.7199} + \left( 1 - (1.3276)3^{-\frac{1.7199}{2}} \right) \quad (4.15)$$

The constant term ensures that, for the uniaxial case, the strain ratio takes the value of one. The important parts of this equation are the power law relationship and the value of the power determined from the fit. The constants will not carry over to the relationship between  $d\psi$  and  $\xi/f'_c$ ;  $\psi_{peak}$  is the integral of  $d\psi$  up to the peak stress, whereas the axial strain at peak stress is the integral of the axial strain. Thus, the constants will be combined with other coefficients in the integration of  $\overline{d\epsilon_p}$  when calculating the relationship between  $d\psi$  and  $\xi/f'_c$ . These coefficients are represented by the introduction of the parameters  $\phi$  and  $\alpha$ . The final equation for  $d\psi$ , given by Equation 3.5, is also shown in Equation 4.16. The power law functional form was used to determine the form of Equation 3.5, and the value of the power in Equation 4.15 is an estimate of  $\gamma$  in Equation 3.5. This value for  $\gamma$  was used to validate the model

(Chapter 6) and predict concrete behavior (Chapter 7).

$$d\psi = \frac{\overline{d\epsilon^p}}{\phi + \alpha\left(\left|\frac{\xi}{f_c'}\right|^\gamma\right)} \quad (4.16)$$

## 4.5 Correlation of the Failure Surface and Flow Rule Parameters

Four of the five remaining parameters,  $\phi$ ,  $\alpha$ ,  $\psi_{peak}$ , and  $\kappa$ , relate to the definition of the failure surface. The final parameter,  $\omega$ , is used in the definition of the flow rule. Due to the nature of these parameters, it is not possible to directly measure them through test data. To further complicate the estimation of these parameters, their values are inter-related. More than one parameter can affect a particular concrete behavior in a similar way, and the nature of this behavior can change with the values of other parameters.

The process chosen to determine values for these parameters was to observe their effect on the shape of the stress versus strain curve of the concrete under different loadings, and visually determine the best choices for these parameters. Due to the somewhat subjective and iterative nature of this process, a limited set of test data representative of typical concrete behavior was chosen to estimate these parameters. The experiments published in Smith et al. (1989), Candappa et al. (1999), and Candappa et al. (2001) were utilized for the selection of the remaining five parameters. Test data from Candappa et al. (1999) and Candappa et al. (2001) were discussed in Section 4.2.1; Smith et al. (1989) were discussed in Section 4.4.1.

These two sets were chosen primarily because of the large strain values to which the experiments were run, and the recording of both axial and lateral strains throughout all experiments. Both sets contained lateral loading magnitudes in the range expected from modern passive confinement methods. While testing was performed outside of the expected range, only data with confinement pressures that could be reached by passive confinement were used.

An additional reason these two sets were chosen was the values of their concrete compressive strengths. As mentioned in Sections 4.2.1, 4.3.1, and 4.4.1, test data show that the increase in the ductility and strength of concrete brought about by confinement is different for normal- versus high-strength concrete. The current model does not explicitly take this effect into account. Thus, it was decided that these parameters would be chosen to best represent normal-strength concrete due to it being most prevalent in modern construction. If modeling of high-strength concrete is desirable, these parameters could instead be determined using high-strength concrete, or the model could be altered to include the effects of high- versus normal-strength concrete at a later time. However, within this thesis, the parameters were chosen based on the results of Smith et al. (1989) for concrete with a compressive strength of 5.0 ksi (34.5 MPa) and the results of Candappa et al. (1999) and Candappa et al. (2001) for concrete with a compressive strength of 6.1 ksi (41.9 MPa). Test data to large strains containing both axial and lateral strains for concrete strengths of 3.0 to 4.0 ksi (21 to 28 MPa) could not be found, so these two were selected as the closest available data to normal-strength concrete.

Results of the 5.0 ksi (34.5 MPa) concrete tested in Smith et al. (1989) are shown in Figure 4.26. Results of the 6.1 ksi (41.9 MPa) concrete tested in Candappa et al. (1999) and Candappa et al. (2001) are shown in Figure 4.27. Note that neither of these data sets were used in determining the residual surface. This is due to the fact that, with one exception, none of the curves extended to the point where the final slope was less than 2% of the initial slope of the curve. However, due to the fact that the parameters being determined in this section affect the entire stress versus strain curve, not simply the post-peak behavior, it is not critical that the residual stress be reached in order to properly estimate these five parameters.

The curves that actually met the residual surface criterion are the curves from Smith et al. (1989) for a confining pressure of 1000 psi (6.9 MPa). From Figure 4.26, it can be seen that those particular curves are actually exhibiting strain hardening at their final behavior, which is not expected or typically seen for concrete in that area of the curve. Thus, the residual stress may not have actually been reached, as

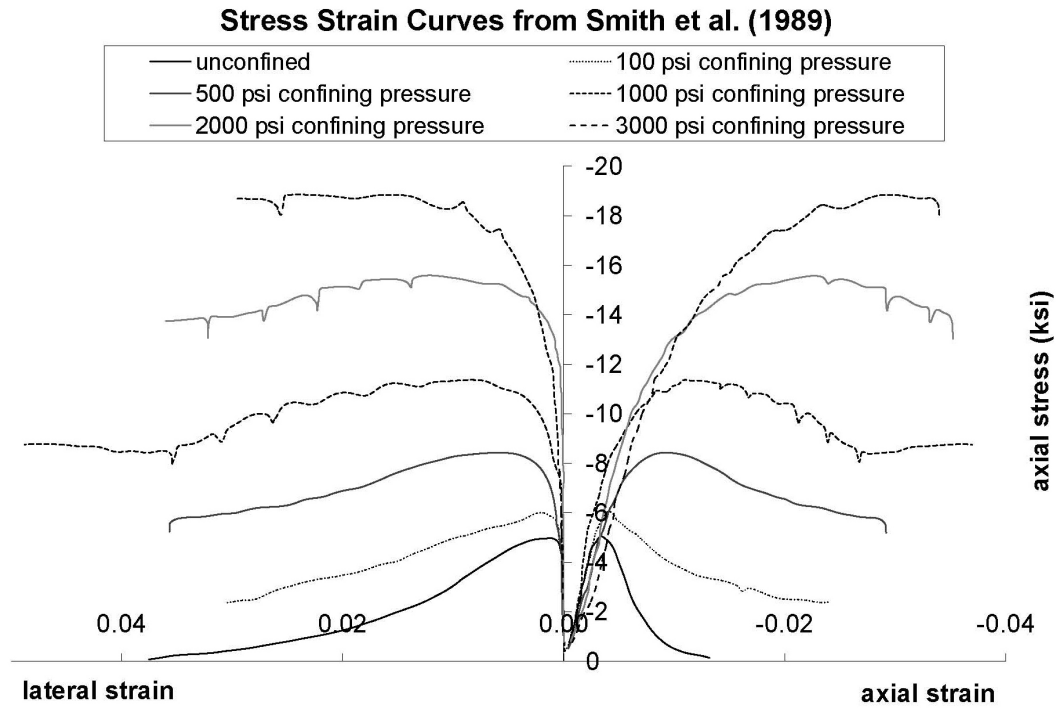


Figure 4.26: Test data for 5.0 ksi (34.5 MPa) concrete from Smith et al. (1989).

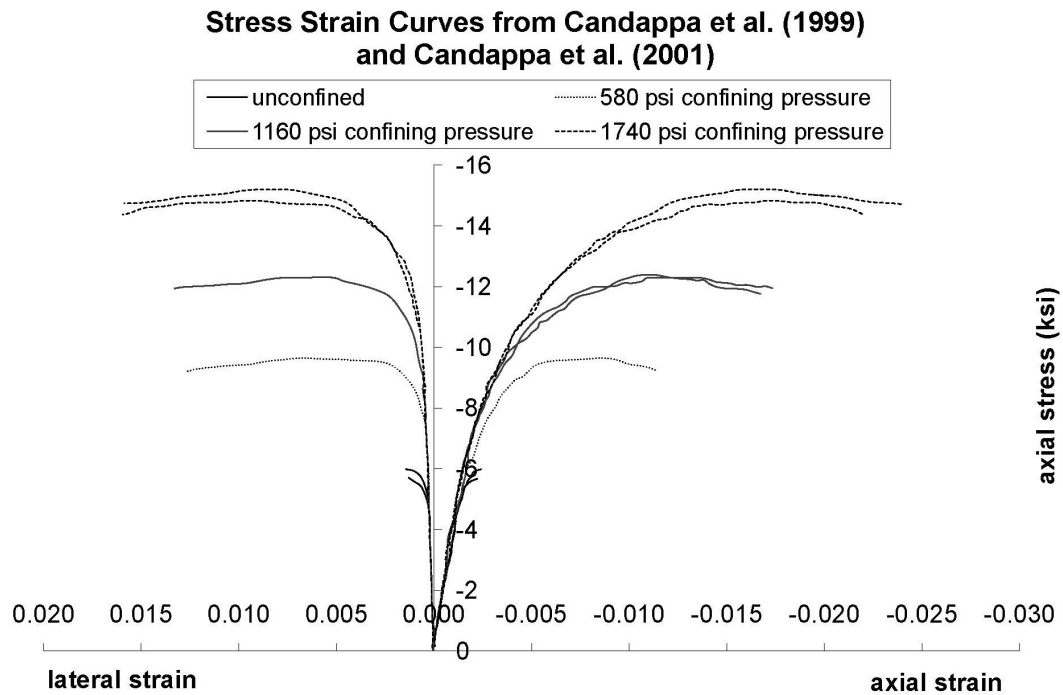


Figure 4.27: Test data for 6.1 ksi (41.9 MPa) concrete from Candappa et al. (1999) and Candappa et al. (2001).

there may be some problem with that particular specimen. Regardless, the general trend of both of these sets of data fall well in line with the majority of concrete data. Therefore, it is acceptable to choose these as being representative of the change in the stress versus strain curve with confinement.

The stress versus strain curves predicted by the model were generated using a special case of the procedure detailed in Chapter 5. A single solid element was used, with the prescribed pressure applied laterally to the element. The axial displacement was then monotonically increased until the axial strain reached that of the corresponding data.

Using the two data sets, the final five parameters were determined by visually matching the model to the data. The values for these last five parameters are given in Table 4.5. The precision of these variables is limited due to the method by which

Table 4.5: Summary of failure surface and flow rule parameter values.

Parameter	Value	Parameter	Value
$\phi$	0.5	$\alpha$	10.
$\psi_{peak}$	$0.6 \times 10^{-3}$	$\kappa$	0.6
$\omega$	0.5		

they were estimated. A comparison of the finalized model to the Smith et al. (1989) data is shown in Figure 4.28. Similarly, Candappa et al. (1999) and Candappa et al. (2001) data are compared to the final model in Figure 4.29.

The model appears to predict reasonably well results at low confining pressures. At very low levels of confinement [below 500 psi (3.4 MPa) for Smith et al. (1989)], strain softening may be a bit too rapid, but at slightly higher levels, the model follows the data more closely. The model is quite successful at predicting the data from Candappa et al. (1999) and Candappa et al. (2001). The results for Smith et al. (1989) are not as close. However, the model does well in the lower confinement range. The ratio of lateral strain to axial strain appears to be working well in the model, which is an important component if passive confinement is to be correctly modeled. Overall, the model is able to predict the behavior of confined concrete throughout the entire loading history.

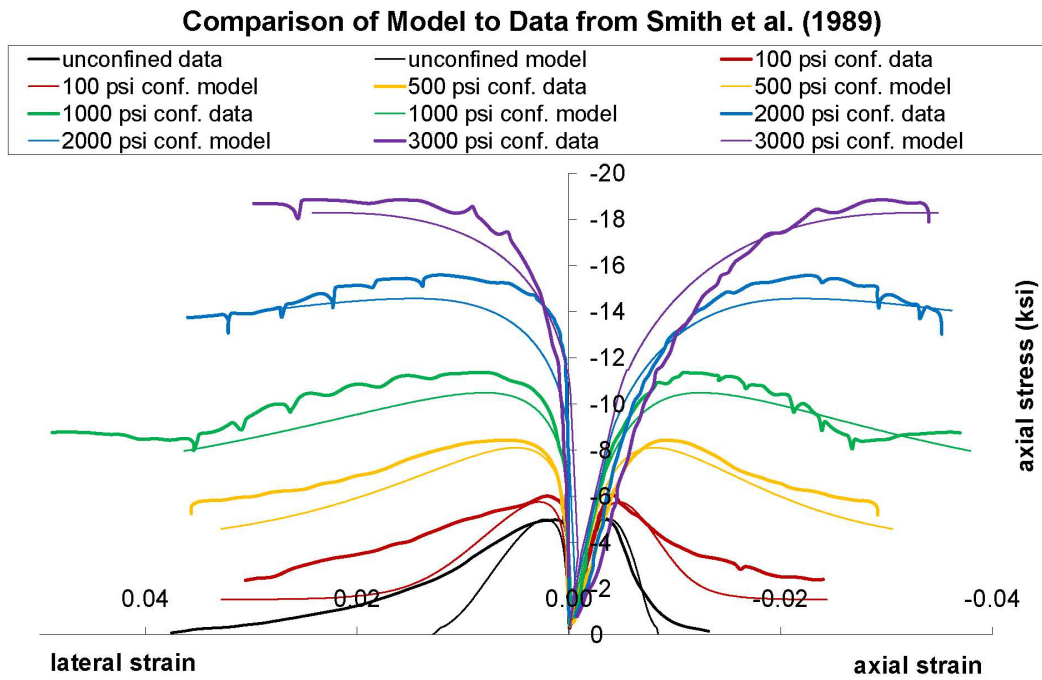


Figure 4.28: Comparison of model to data from Smith et al. (1989).

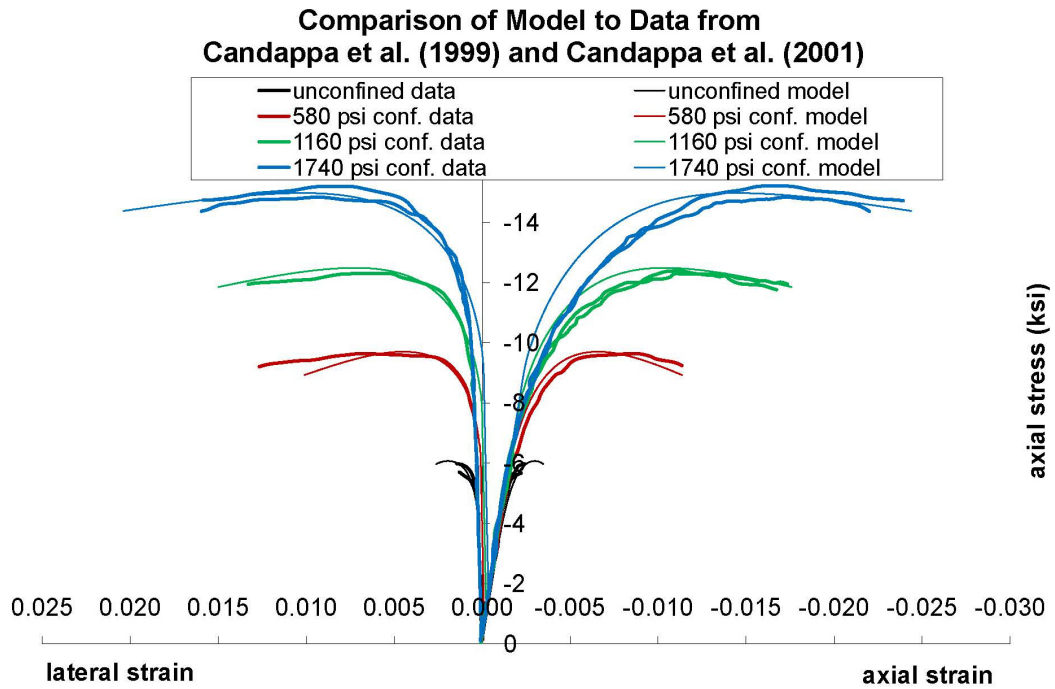


Figure 4.29: Comparison of model to data from Candappa et al. (1999) and Candappa et al. (2001).

## 4.6 Summary of Parameters

Table 4.6 shows the final values for the twenty-four parameters of the concrete plasticity model. These values were implemented into a finite element program to predict the behavior of confined concrete.

Table 4.6: Summary of model parameter values.

Parameter	Value	Parameter	Value
$c$	1.1333	$d$	1.7816
$a_{0,peak}$	0.0	$b_{0,peak}$	0.0
$a_{1,peak}$	-1.4344	$b_{1,peak}$	-1.9711
$a_{2,peak}$	0.0924	$b_{2,peak}$	0.3103
$a_{3,peak}$	1.1005	$b_{3,peak}$	0.7039
$a_{0,residual}$	0.0	$b_{0,residual}$	0.0
$a_{1,residual}$	-0.9764	$b_{1,residual}$	-1.3417
$a_{2,residual}$	0.0565	$b_{2,residual}$	0.1898
$a_{3,residual}$	1.4833	$b_{3,residual}$	0.9847
$\gamma$	1.7199	$\phi$	0.5
$\alpha$	10.	$\psi_{peak}$	$0.6 \times 10^{-3}$
$\kappa$	0.6	$\omega$	0.5